Monthly Notices
of the
ROYAL ASTRONOMICAL SOCIETY

MNRAS **500,** 2741–2756 (2021)
Advance Access publication 2020 November 05

doi:10.1093/mnras/staa3412

Connecting cosmological accretion to strong Ly α absorbers

Tom Theuns ★

Institute for Computational Cosmology, Department of Physics, Durham University, Durham DH1 3LE, UK

Accepted 2020 October 28. Received 2020 October 27; in original form 2020 September 24

ABSTRACT

We present an analytical model for the cosmological accretion of gas on to dark matter haloes, based on a similarity solution applicable to spherical systems. Performing simplified radiative transfer, we compute how the accreting gas turns increasingly neutral as it self-shields from the ionizing background, and obtain the column density, $N_{\rm H\,I}$, as a function of impact parameter. The resulting column-density distribution function (CDDF) is in excellent agreement with observations. The analytical expression elucidates (1) why haloes over a large range in mass contribute about equally to the CDDF as well as (2) why the CDDF evolves so little with redshift in the range $z = 2$–5. We show that the model also predicts reasonable damped Lyman-αabsorber (DLA) line widths (v_{90}), bias, and molecular fractions. Integrating over the CDDF yields the mass density in neutral gas, $\Omega_{\rm H\,I}$, which agrees well with observations. $\Omega_{\rm H\,I}(z)$ is nearly constant even though the accretion rate on to haloes evolves. We show that this occurs because the fraction of time that the inflowing gas is neutral depends on the dynamical time of the halo, which is inversely proportional to the accretion rate. Encapsulating results from cosmological simulations, the simple model shows that most Lyman-limit systems and DLAs are associated with the cosmological accretion of gas on to haloes.

Key words: galaxies: high-redshift – intergalactic medium – quasars: absorption lines.

1 INTRODUCTION

Ultraviolet (UV) photons emitted by a cosmologically distant source, such as a quasar, may be absorbed en route by scattering off neutral hydrogen atoms in the Lyman ($n = 1 \rightarrow n'$) or Lyman-limit ($n = 1 \rightarrow \infty$) transitions (n and n' are the hydrogen atom's principal quantum number). This generates a series of absorption lines due to intervening 'Lyman-α' clouds. The spectral signature when many lines are close together and overlap is that of a 'forest' of lines, hence the name 'Lyman-α forest' (Weymann, Carswell & Smith 1981). The taxonomy of these lines depends on how column density, $N_{\rm H\,I}$, is determined. When $N_{\rm H\,I}$ is sufficiently small, absorption lines have a nearly Gaussian shape that can be fitted accurately with a Voigt profile. Lines become increasingly square in shape and insensitive to $N_{\rm H\,I}$ with increasing $N_{\rm H\,I}$, but once $N_{\rm H\,I} \gtrsim 10^{17.2}\,{\rm cm}^{-2}$, the Lyman-limit optical depth is so high that the presence of the absorber results in a strong depression of the flux below $(1 + z) \times 912$ Å, where z is the absorber's redshift. Finally, at even higher values of $N_{\rm H\,I} \geq 10^{20.3}\,{\rm cm}^{-2}$, absorption is so strong that the line shape can be measured far from the line centre where it is dominated by the natural line width of the Lyman-α transition. The Lorentzian shape of this natural line profile leads to such high $N_{\rm H\,I}$ absorbers to be called 'damped Lyman-α absorbers' (DLAs), in analogy with the Lorentzian shape of the resonance of a damped harmonic oscillator (Beaver et al. 1972; Wolfe et al. 1986). Lines are therefore classified based on column density as Lyman-α forest, Lyman-limit system (LLS), and DLAs for $N_{\rm H\,I} < 10^{17.2}$, $<10^{20.3}$, and $\geq 10^{20.3}\,{\rm cm}^{-2}$, respectively (see e.g. Rauch 1998; Péroux & Howk 2020, for reviews). This paper focuses on DLAs, foraying briefly into the realm of LLSs.

The original motivation for studying DLAs by Wolfe et al. (1986) was to identify high-redshift galaxies. Indeed, a sightline through the Milky Way's disc is likely to have $N_{\rm H\,I} \geq 10^{20.3}\,{\rm cm}^{-2}$; therefore, a sightline through a high-z Milky Way-like galaxy would likely result in a DLA in the spectrum of a background quasar – and, of course, high-redshift DLAs were already known and detectable back then. This realization inadvertently initiated decades of relatively unsuccessful attempts to identify optical counterpart(s) to DLAs (with some exceptions, e.g. Møller, Fynbo & Fall 2004; Fynbo et al. 2010; Péroux et al. 2012; Fumagalli et al. 2015). The low success rate of such searches was attributed to the DLA galaxies being generally too faint to be detectable (see e.g. the discussion by Krogager et al. 2017). This endeavour has been revolutionized by the advent of integral field units that allow for the identification of faint galaxies at a range of distances from the sightline to the quasar in a single telescope pointing (e.g. Péroux et al. 2016 using SINFONI; Fumagalli et al. 2017; Mackenzie et al. 2019 using MUSE). Such studies suffer from the opposite problem: There may be several galaxies detected close to the sightline at similar redshift as the DLA, in which case it becomes unclear which particular galaxy – if any – to associate with the DLA.

The prevailing view that DLAs are gas closely associated with a galaxy was also the motivation for several theoretical models (e.g. Maller et al. 2001; Fynbo et al. 2008; Di Gioia et al. 2020; Krogager et al. 2020). Typically, these struggle to reproduce the observed number density of DLAs for a realistic value of size of the galaxy. In the relatively few cases where a galaxy is identified with a particular DLA, it is not unusual for the impact parameter to be $b > 10$ kpc (and sometimes much larger than that, e.g. Fumagalli et al. 2017), and that is of course (much) larger than the sizes of (stellar components of)

★ E-mail: tom.theuns@durham.ac.uk

high-z galaxies, which are closer to ∼3 kpc even for massive galaxies (e.g. van der Wel et al. 2014).

DLAs are relatively rare, with of the order of ∼0.3 DLA per decade in column density per redshift interval $\Delta z = 1$ at $z = 3$. Statistically robust studies of DLAs, especially at high $N_{\rm H\,I}$, have been revolutionized by the advent of very large samples of quasar spectra [see, for example, DLAs identified by Noterdaeme et al. (2012) in the Sloan Digital Sky Survey (SDSS) data release (DR) 9 and Ahn et al. (2012), or by Ho, Bird & Garnett (2020) in SDSS DR12 and Alam et al. (2015)]. Whereas earlier numerical simulations (e.g. Nagamine, Springel & Hernquist 2004; Tescari et al. 2009) and cosmological zoom simulations (e.g. Pontzen et al. 2008) reproduced the earlier data by Péroux et al. (2001) and Prochaska, Herbert-Fort & Wolfe (2005) relatively well, the leap in data brought about by the SDSS made it harder for simulations to reproduce the data.

Nevertheless, several relatively recent simulations can reproduce the vastly improved DLA statistics reasonably well (e.g. Altay et al. 2011; Cen 2012; Bird et al. 2014). The simulations differ in numerical technique (particle based, grid based, and moving mesh, respectively) and vary the prescriptions associated with the formation of the galaxy (both how stars form and importantly in the way that feedback is implemented). What these simulations have in common is that the majority of the DLA cross-section is not associated with the stellar component of the galaxy, but rather the gas that gives rise to the DLA is distributed throughout and even outside the galaxy's halo ('every galaxy is a DLA, but not every DLA is a galaxy'), typically in the form of several filaments of high-density gas, as also seen in the high-resolution zoom simulations of Fumagalli et al. (2011) and Faucher-Giguère & Kereš (2011). In the simulations presented by van de Voort et al. (2012), the majority of the gas associated with LLSs and DLAs at redshift $z \sim 3$ is falling rapidly towards the central galaxy of a dark matter halo while remaining cool (temperature $T \lessapprox 10^{5.5}$ K). As it accretes on to the galaxy, the majority of gas is ejected in the form of a galactic outflow powered by supernovae. Gas inside the galaxy that is neither inflowing nor outflowing and the outflow itself add a small contribution to the total DLA cross-section.

Two aspects of these simulations form the motivation for the analytical model described here. First, the DLA gas is mostly accreting towards the centre of dark matter haloes (van de Voort et al. 2012); therefore, our model is based on cosmological accretion [rather than assuming that DLA gas is in centrifugal or hydrostatic equilibrium in a halo as in the model by Padmanabhan, Choudhury & Refregier (2016) or is associated directly with galaxies, as in the recent models by Krogager et al. (2020) and Di Gioia et al. (2020)]. We will assume that the accretion is mostly smooth (as opposed to accretion via satellites, say), an idea supported by simulations (e.g. Crain et al. 2017; Wright et al. 2020), at least at higher $z \gtrapprox 1$, say. Both assumptions are consistent with the 'cold accretion' paradigm of Kereš et al. (2005) and Dekel et al. (2009). Secondly, although the importance of feedback from the galaxy on DLAs is somewhat contested (e.g. Sommer-Larsen & Fynbo 2017; Rhodin et al. 2019), the simulations by Altay et al. (2013) that are based on the OWLS project described by Schaye et al. (2010) include a very wide variety of feedback implementations and show convincingly that outflows driven by feedback affect DLA statistics mostly at the high-column-density end, $N_{\rm H\,I} \gtrapprox 10^{21.5}\,{\rm cm}^{-2}$. This encourages us to simply neglect feedback, either from outflows or indeed from local ionizing radiation that may play a role at the high-column-density end (e.g. Rahmati et al. 2013). Obviously, this is only an approximation. As stressed by Krogager et al. (2017), correlations between DLAs and galaxies depend on metallicity: Since we neglect feedback, we cannot study this interesting observational finding. A third motivation for developing an analytical model is to elucidate why the DLA column-density distribution function (CDDF) evolves so weakly with redshift (as observed and reproduced by simulations) and why haloes with a range of masses contribute about equally to the CDDF. Having an analytical expression for the CDDF makes this straightforward.

This paper is organized as follows: The model is described in Section 2, which starts by discussing the radial distribution of gas accreting on to haloes and goes on to derive the resulting CDDF. Section 3 presents in more detail the validity of some of the assumptions and where improvements could be made. Finally, Section 4 presents summary and conclusions. We will use the Planck Collaboration XVI (2014) values of the cosmological parameters where needed.

2 THE MODEL

Our model for connecting DLAs to dark matter haloes has several ingredients and makes many simplifying assumptions. It is described in Section 2.1, which starts by relating the radial and column-density distribution of neutral gas to a halo of a given mass at a given z, and explores the differential contribution of haloes of a given mass to the CDDF. We explain there why a relatively extended range in halo masses contributes significantly to the CDDF. Next, we calculate the CDDF in Section 2.2 and use the analytical expression to explore its redshift evolution. The dynamics of the gas is examined in terms of DLA bias in Section 2.3 and in terms of line widths in Section 2.4. We explore the molecular contents of DLAs in Section 2.5, and the cosmological fraction of gas in DLAs in Section 2.6.

2.1 Cosmological accretion on to haloes

The equations describing cosmological accretion on to a spherically symmetric overdensity associated with a dark matter halo admit a similarity solution in the case of an Einstein–de Sitter (EdS) universe[1] (Bertschinger 1985). In this solution, the density profile is a power law, $\rho(r) \propto r^{-\alpha}$, over a large range in radii r. The value of the exponent, α, depends on whether the accreting material is collisional or collisionless and on the inner boundary condition and is in the range $\alpha \sim 1.5$–2.2. We will assume here that accreting gas remains cool while accreting (in fact, we will assume that it remains isothermal), and as it enters the interstellar medium of the galaxy, it cools rapidly so that the accretion shock does not propagate outwards. Under these assumptions, α is at the steeper end of the range: We will pick $\alpha = 2.2$ for making figures. Hydrodynamical simulations show that the assumptions on the thermal evolution of the accreting gas are reasonable, at least for sufficiently low-mass haloes; see, for example, the density–temperature diagram of gas at overdensities $\rho/\langle\rho\rangle$ in the range 10–100 in fig. 2 of Theuns et al. (1998).

We set the normalization of the density profile by requiring that the mean density within the halo's virial radius, $R_{\rm h}$, is 200 times the critical density (e.g. Mo, Mao & White 1998). To calculate the corresponding density profile of hydrogen gas,[2] we assume that the accreting mass has its cosmological share of baryons, so that the ratio of gas over total matter is $\omega_{\rm b} = \Omega_{\rm b}/\Omega_{\rm m}$, and that the

[1]For studying structure formation at redshift $z \gtrapprox 1$, an EdS model should be sufficiently accurate.

[2]We will use a subscript 'h' to denote properties of a halo, and subscript 'H' to denote properties that refer to hydrogen.

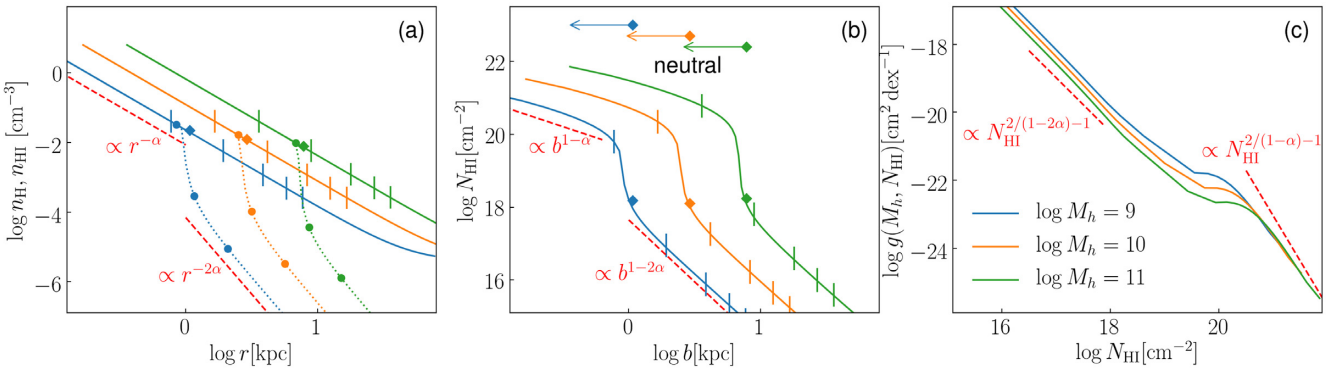

Figure 1. Gas profiles of dark matter haloes at redshift $z = 3$ for $\alpha = 2.2$. (a): Radial profiles of the total hydrogen density $n_{\rm H}$ (solid lines) and neutral hydrogen density $n_{\rm H\,I}$ (dotted lines) computed by integrating equation (3) numerically, for different halo masses (different colours as per the legend in panel c). Thin vertical lines are drawn at fractions 0.1, 0.25, 0.5, 0.75, and 1 of the viral radius $R_{\rm h}$ of the halo; solid dots are drawn at locations where the optical depth reaches $\tau = 10$, 1, and 0.1 (from the inside out); the filled diamond is drawn at the approximate location of the ionization front $r_{\rm I}$ from equation (8). Power-law profiles are drawn as red dashed lines. (b): Corresponding column density, $N_{\rm H\,I}$, as a function of impact parameter b. Thin vertical lines are drawn where b equals a fraction of 0.1, 0.25, 0.5, 0.75, and 1 of the viral radius $R_{\rm h}$ of the halo; red dashed inner and outer lines indicate power laws, $N_{\rm H\,I} \propto b^{1-\alpha}$ and $\propto b^{1-2\alpha}$; filled diamonds are drawn at the location of $r_{\rm I}$, with additionally arrows pointing inwards from where the gas is mostly neutral. (c): Contribution of such haloes to the column-density distribution from equation (10). The red dashed inner and outer lines indicate power laws with the slopes expected from the dependence of the cross-section on column density (see the text). In all three panels, profiles are coloured by the logarithm of the halo mass, $M_{\rm h}$, in solar masses, as per the legend in panel (c).

hydrogen abundance by mass has its primordial value, X. Under these assumptions,

$$n_{\rm H}(r) = n_{\rm H,0}\left(\frac{R_{\rm h}}{r}\right)^{\alpha};\quad n_{\rm H,0} = X\,\omega_{\rm b}\,\frac{\rho_{\rm h}}{m_{\rm H}};\quad \rho_{\rm h} \approx \frac{200}{3}\rho_{\rm c}. \tag{1}$$

Here, $m_{\rm H}$ is the mass of a hydrogen atom and $n_{\rm H,0}$ is the hydrogen number density at the virial radius[3]; in the figures, we use the Planck Collaboration XVI (2014)'s values of the cosmological parameters. In practice, we add the mean density to $n_{\rm H}$, to avoid the halo's density falling below the mean.[4]

The cosmological growth of a dark matter halo is described by

$$M_{\rm h}(z) = M_{\rm h,0}\,m_{\rm h}(z);\quad m_{\rm h}(z) = (1+z)^a\,\exp(-bz), \tag{2}$$

where $M_{\rm h}$ is the virial mass of the halo at redshift z, $M_{\rm h,0}$ is the mass of the halo at $z = 0$, and $a \approx 0.24$ and $b \approx 0.75$ are fits by Correa et al. (2015a, b) to simulations.

Given the total hydrogen profile, we proceed to compute the *neutral* hydrogen density profile, $n_{\rm H\,I}(r)$. The ionizing radiation from the UV background will photoionize the intergalactic medium (IGM) as well as gas in the outskirts of the halo. As the gas gets denser, the optical depth to the ionizing radiation increases, and eventually hydrogen starts to self-shield. To describe this, we assume that (1) hydrogen is in photoionization equilibrium at a constant temperature of $T = 10^4$ K, (2) collisional ionization can be neglected, (3) the presence of helium and all other elements can be neglected, (4) the frequency dependence of the photoionization cross-section can be neglected, and (5) the optical depth can be approximated by its value in a slab (rather than spherical) geometry.[5] Under these assumptions, the neutral hydrogen fraction, x, at radius r, is given by

$$x(r) \equiv \frac{n_{\rm H\,I}(r)}{n_{\rm H}(r)} = \frac{\alpha_{\rm B}}{\Gamma(r)} n_{\rm H}(r)$$

$$\Gamma(r) = \Gamma_0 \exp(-\tau(r))$$

$$\tau(r) = \sigma_{\nu_{\rm th}} \int_r^\infty x(r')\,n_{\rm H}(r')\,{\rm d}r', \tag{3}$$

where[6] $\alpha_{\rm B}$ is the 'case-B' recombination coefficient evaluated at a temperature of $T = 10^4$ K, $\sigma_{\nu_{\rm th}}$ is the photoionization cross-section at the ionization threshold, and Γ_0 is the value of the photoionization rate in the IGM, for which we will take the values as a function of redshift computed by Haardt & Madau (2012). Rather than performing the integral for the optical depth to infinity, we integrate inwards from $r = 10 \times R_{\rm h}$, setting $\Gamma = \Gamma_0$ at $r = 10 \times R_{\rm h}$. Since the gas is highly ionized outside $R_{\rm h}$, the exact value taken for this integration limit is mostly irrelevant, provided it is larger than $R_{\rm h}$. Obtaining the run of x versus r numerically is straightforward; it is also easy to understand the result: In the outskirts of the halo, the gas is highly ionized so that $\tau \approx 0$. Once $\tau \approx 1$, the reduction in ionizing flux $\propto \exp(-\tau)$ increases very rapidly with decreasing r; hence, the neutral fraction increases rapidly from very small to $x \approx 1$ over the narrow extent of the ionization front. Inside the front, $x \approx 1$. Therefore, we expect that

$$\begin{cases} x(r) \approx (\alpha_{\rm B}/\Gamma_0) n_{\rm H}(r) \rightarrow n_{\rm H\,I}(r) \approx (\alpha_{\rm B}/\Gamma_0)\,n_{\rm H}(r)^2 & \text{for } r > r_{\rm I} \\ x(r) \approx 1 \rightarrow n_{\rm H\,I}(r) \approx n_{\rm H}(r), & \text{for } r < r_{\rm I}, \end{cases} \tag{4}$$

where $r_{\rm I}$ is the location of the ionization where $\tau \approx 1$. The value of $r_{\rm I}$ can be estimated in the slab geometry by using the first expression

[3]The factor 200/3 that relates $\rho_{\rm h}$ to the value of the critical density, $\rho_{\rm c}$, assumes that $\alpha = 2$ rather than our preferred value of 2.2. The steeper profile leads to an apparent divergence of the enclosed mass at the centre. However, in reality, the power-law profile ceases to hold inside the accretion shock. Such a normalization should be approximately consistent with the similarity solution.

[4]This has a minor effect that can just be noticed outside the virial radius of the $M_{\rm h} = 10^9$ M$_\odot$ halo in Fig. 1.

[5]See Zheng & Miralda-Escudé (2002) and Sykes et al. (2019) for calculations in spherical geometry.

[6]We take $\alpha_{\rm B} = 1.269 \times 10^{-13}\,\eta^{1.503}/(1+(\eta/0.522)^{0.407})^{1.923}$ cm^3 s^{-1}, where $\eta = 315\,614\,{\rm K}/T$ with $T = 10^4$ K and $\sigma_{\nu_{\rm th}} = 6.63 \times 10^{-18}$ cm^2.

for the neutral hydrogen density, and solving $\sigma_{\rm th}\int_{r_{\rm I}}^{10R_{\rm h}} n_{\rm HI}(r')\,{\rm d}r' = \tau_{r_{\rm I}} = 1$ for $r_{\rm I}$, as we discuss in more detail below.

The run of total density and neutral hydrogen density obtained by numerically integrating equation (1) together with equation (3) for haloes with a range of masses is shown at redshift $z = 3$ in panel (a) of Fig. 1, where the solid lines show $n_{\rm H}(r)$ and the dotted lines show $n_{\rm HI}(r)$; different colours correspond to different halo masses. As expected, $n_{\rm HI} \approx n_{\rm H}$ close to the centre, and $n_{\rm HI} \propto n_{\rm H}^2$ in the outskirts: The innermost red dashed line is $\propto n_{\rm H}$ and the outermost red dashed line is $\propto n_{\rm H}^2$ to guide the eye. The location of the ionization front occurs where $\tau \approx 1$ as expected; the radius $r_{\rm I}$ of the front is between 0.1 and 0.25 times the virial radius for the haloes shown ($r_{\rm I}/R_{\rm h}$ is smaller for lower mass haloes).

The column density through the neutral gas is

$$N_{\rm HI}(b) = \int_{-\infty}^{\infty} n_{\rm HI}(r=(b^2+z^2)^{1/2})\,{\rm d}z$$
$$= 2\int_b^{\infty} n_{\rm HI}(r)\frac{r}{(r^2-b^2)^{1/2}}\,{\rm d}r, \quad (5)$$

where b is the impact parameter; in practice, we use $10\,R_{\rm h}$ for the upper integration limit rather than infinity. Since $n_{\rm HI}(r)$ is to a good approximation a power law, $n_{\rm HI}(r) \approx r^{-\beta}$ (where $\beta = \alpha$ for $r < r_{\rm I}$ and $\beta = 2\alpha$ for $r > r_{\rm I}$), we expect that approximately

$$N_{\rm HI}(b) \approx 2\,n_0\,b^{1-\beta}\,R_{\rm h}^{\beta}\int_0^{\infty}\frac{1}{(1+y^2)^{\beta/2}}\,{\rm d}y \approx b^{1-\beta}\,R_{\rm h}^{\beta}, \quad (6)$$

that is, also a power law in b, with the dependence on halo mass a power law as well, since $R_{\rm h} \propto M_{\rm h}^{1/3}$. Here, $n_0 = x\,n_{\rm H}$ with x the neutral fraction at the virial radius for $r > r_{\rm I}$, and $x = 1$ for $r < r_{\rm I}$, as in equation (4). $N_{\rm HI}(b)$, integrated numerically, is shown in panel (b) of Fig. 1 for the haloes shown in panel (a); the power-law relation captures the shape of the $N_{\rm HI}$ profile well, as expected. Notice also that $N_{\rm HI}$ increases rapidly by a factor of several hundred at the location of the ionization front, $r = r_{\rm I}$, where x changes rapidly from $x \ll 1$ to $x \approx 1$.

We estimate the approximate location of the ionization front, $r_{\rm I}$, by assuming that the gas outside $r_{\rm I}$ is highly ionized as in equation (4). Integrating from $r_{\rm I}$ outwards, the optical depth to infinity is

$$\tau_{\rm I} = \sigma_{\nu_{\rm th}}\int_{r_{\rm I}}^{\infty} n_{\rm HI}\,{\rm d}r = \frac{\sigma_{\nu_{\rm th}}\,\alpha_{\rm B}}{\Gamma_0}\int_{r_{\rm I}}^{\infty} n_{\rm H}(r)^2\,{\rm d}r$$
$$= \frac{\sigma_{\nu_{\rm th}}\,\alpha_{\rm B}\,n_{\rm H,0}^2}{\Gamma_0\,(2\alpha-1)}\left(\frac{R_{\rm h}}{r_{\rm I}}\right)^{2\alpha-1}R_{\rm h} \sim 1, \quad (7)$$

so that

$$r_{\rm I} = \left(\frac{\sigma_{\nu_{\rm th}}\alpha_{\rm B}\,n_{\rm H,0}^2\,R_{\rm h}}{(2\alpha-1)\Gamma_0}\right)^{1/(2\alpha-1)}R_{\rm h}. \quad (8)$$

The locations corresponding to this value of $r_{\rm I}$ are indicated in Fig. 1 using filled diamonds. Defined in this way, the column density measured outwards from $r_{\rm I}$ to infinity is $N_{\rm HI} = \tau/\sigma_{\rm th}$ with $\tau = 1$, corresponding to $\log N_{\rm HI}[{\rm cm}^{-2}] \approx 17.2$ – the characteristic column density of LLSs. However, the column density of the halo for $b = r_{\rm I}$ is of course a bit higher because of the different geometry of the two sightlines: radially outwards for the definition of $r_{\rm I}$ versus hitting the absorber at a given impact parameter for an absorber.

We can use the $N_{\rm HI}$–b relation to compute the cross-section, $\sigma(N_{\rm HI})$, within which the column density is larger than some value, $\sigma = \pi b^2 \propto N_{\rm HI}^{2/(1-\beta)}$. Its derivative, ${\rm d}\sigma/{\rm d}N_{\rm HI}$, is closely related to the shape of the CDDF, $f(N_{\rm HI})$. To see this, we start from the average number of times, ${\rm d}N$, that a sightline with proper length ${\rm d}l$ intersects absorbers with proper cross-section σ and co-moving number density $n(z)$:

$${\rm d}N = n(z)\,(1+z)^3\,\sigma\,{\rm d}l = n(z)\,(1+z)^3\,\sigma\,\frac{c\,{\rm d}z}{(1+z)H(z)}$$
$$\equiv \frac{c}{H_0}\,n(z)\,\sigma\,{\rm d}X$$
$${\rm d}X \equiv \frac{H_0(1+z)^2}{H(z)}\,{\rm d}z, \quad (9)$$

where $H(z)$ is the Hubble constant at redshift z, $H_0 = H(z=0)$, and the dimensionless quantity ${\rm d}X$ is called the 'absorption distance'; the factor $(1+z)^3$ converts the co-moving density of absorbers, $n(z)$, into a proper number density [Bahcall & Peebles (1969) or see, for example, Fumagalli et al. (2011), Section 5.1]. Therefore, the number of times a sightline intersects an absorber with a given column density, due to a halo with a given mass per dex in halo mass, is given by

$$g(M_{\rm h}, N_{\rm HI}) \equiv \frac{{\rm d}^3N}{{\rm d}N_{\rm HI}{\rm d}\log M_{\rm h}{\rm d}X} = \frac{c}{H_0}\frac{{\rm d}n}{{\rm d}\log M_{\rm h}}\frac{{\rm d}\sigma(M_{\rm h}, N_{\rm HI})}{{\rm d}N_{\rm HI}}. \quad (10)$$

In this paper, we use the COLOSSUS PYTHON package described by Diemer (2018) to compute the number density of haloes per dex in halo mass (the halo mass function) ${\rm d}n/{\rm dlog}\,M_{\rm h}$, stipulating a cosmology with the cosmological parameters from Planck Collaboration XVI (2014). We selected the Reed et al. (2007) fitting function to the mass function as implemented in COLLOSUS.

The CDDF – the number of absorbers with a given column density per absorption distance ${\rm d}X$ – is the integral of the function g over halo mass,

$$f(N_{\rm HI}) \equiv \frac{{\rm d}^2N}{{\rm d}N_{\rm HI}{\rm d}X} = \int_{-\infty}^{\infty} g(M_{\rm h}, N_{\rm HI})\,{\rm d}\log M_{\rm h}. \quad (11)$$

The contribution of haloes of given mass to the CDDF, $g(M_{\rm h}, N_{\rm HI})$, is plotted in panel (c) of Fig. 1. Its dependence on column density is due to the factor ${\rm d}\sigma(M_{\rm h}, N_{\rm HI})/{\rm d}N_{\rm HI} \propto N_{\rm HI}^{-2/(\beta-1)-1}$, with the power-law approximation shown by red dashed lines.[7] The power-law shape of g is therefore a consequence of the power-law profile of the density in the haloes, shown in panel (a), with the change in slope a consequence of the transition from fully neutral in the centre of the haloes, so that $n_{\rm HI}(r) \propto n_{\rm H}(r)$, to the highly ionized regime in the outskirts, where $n_{\rm HI}(r) \propto n_{\rm H}^2(r)$. The inflection around $N_{\rm HI} \sim 10^{20}\,{\rm cm}^{-2}$ occurs when the value of the impact parameter is (approximately) equal to $r_{\rm I}$.

It is striking how at higher values of $N_{\rm HI}$, $N_{\rm HI} \sim 10^{21}\,{\rm cm}^{-2}$ say, the contribution of haloes is almost independent of halo mass over two orders of magnitude in $M_{\rm h}$. The underlying reason for this is as follows: First, we will neglect the contribution of the ionized halo of gas to the column density – this is an excellent approximation at sufficiently high $N_{\rm HI}$. Therefore, at impact parameter $b \ll r_{\rm I}$, we find that

$$N_{\rm HI}(M_{\rm h}, b, z) \approx 2\,n_{\rm H,0}(z)\,R_{\rm h}^{\alpha}(M_{\rm h}, z)\,b^{1-\alpha}\,I$$
$$I \equiv \int_0^{\left((r_{\rm I}(z)/b)^2-1\right)^{1/2}}\frac{{\rm d}x}{(1+x^2)^{\alpha/2}}, \quad (12)$$

[7] As before, β is the slope of the radial neutral hydrogen density profile, $n_{\rm HI} \propto r^{-\beta}$, which is $\beta = \alpha$ when the gas is neutral and $\beta = 2\alpha$ when it is highly ionized.

where we have explicitly written out the redshift dependence for later use. We can solve this equation for the value of the impact parameter b at which a sightline through a halo of mass $M_{\rm h}$ has column density $N_{\rm H\,I}$ or greater, and calculate the corresponding cross-section $\sigma \equiv \pi b^2$,

$$\sigma(N_{\rm H\,I}, M_{\rm h}, z) = \pi \left(2\, n_{\rm H,0}(z)\right)^{2/(\alpha-1)} R_{\rm h}^{2\alpha/(\alpha-1)} \times N_{\rm H\,I}^{-2/(\alpha-1)}\, I^{2/(\alpha-1)}. \quad (13)$$

To gain insight and obtain a simpler analytical scaling relation, we further neglect the somewhat awkward dependence of σ on the integral I, in which case $\mathrm{d}\sigma/\mathrm{d}N_{\rm H\,I} \propto R_{\rm h}^{2\alpha/(\alpha-1)} \propto M_{\rm h}^{2\alpha/3(\alpha-1)}$, where we have used the fact that $n_{\rm H,0}$ depends on redshift but not on $M_{\rm h}$. Finally, we find that the contribution of haloes of mass $M_{\rm h}$ to the CDDF depends on halo mass as

$$g(M_{\rm h}, N_{\rm H\,I} \sim 10^{21}\,{\rm cm}^{-2}) \propto \frac{\mathrm{d}n}{\mathrm{d}\log M_{\rm h}} \frac{\mathrm{d}\sigma}{\mathrm{d}N_{\rm H\,I}} \approx M_{\rm h}^{-1.1}\, M_{\rm h}^{2\alpha/3(\alpha-1)} \approx M_{\rm h}^{0.13}, \quad (14)$$

where we have taken a value of -1.1 for the slope of the halo mass function at low masses at $z = 3$, and our default value of $\alpha = 2.2$ for the slope of the density distribution within a given halo. The contribution of haloes to the CDDF is thus a slowly increasing function of $M_{\rm h}$ at high $N_{\rm H\,I}$, increasing by a factor of $\sim$2 for $M_{\rm h}$ increasing by a factor of 100 from $M_{\rm h} = 10^{10}$ to $10^{12}\,{\rm M}_\odot$. At even higher mass, the contribution eventually drops due to the exponential factor in the halo mass function. The scaling exhibited by equation (14) explains the weak dependence of the CDDF on halo mass. We will verify the scaling in more detail numerically below, including the impact of the integral I.

We could now integrate equation (10) over halo mass to obtain the CDDF, as in equation (11). Before doing so, we should be more careful in considering for which haloes our model assumptions hold. The ionizing background will photoevaporate gas from haloes below some critical mass, $M_{\rm crit}(z)$, and such haloes will not contribute to the CDDF. Here, we will use the values of $M_{\rm crit}(z)$ obtained using numerical simulations by Okamoto, Gao & Theuns (2008). At *high* halo masses, $M_{\rm h} \gg 10^{12}\,{\rm M}_\odot$, on the other hand, a lot of the halo gas is presumably shock heated rather than cold, in which case we should not neglect collisional ionization and additionally the radial density profile is likely to be affected. Fortunately, above $z \sim 2$, such haloes are relatively rare and their contribution to the integral in equation (11) is already exponentially suppressed due to the shape of the halo mass function, meaning that we may not need to further suppress their contribution. We will therefore compute the CDDF as

$$f(N_{\rm H\,I}) \equiv \frac{\mathrm{d}^2 N}{\mathrm{d}N_{\rm H\,I}\mathrm{d}X} = \int_{\log M_{\rm crit}(z)}^{\infty} g(M_{\rm h}, N_{\rm H\,I})\, \mathrm{d}\log M_{\rm h}, \quad (15)$$

where in practice we integrate up to haloes of mass $10^{13}\,{\rm M}_\odot$. There remains one further subtlety regarding the definition of $M_{\rm h}$. To compute the number density of haloes, $\mathrm{d}n/\mathrm{dlog}\,M_{\rm h}$, we use the COLOSSUS routines of Diemer (2018), which are fits to dark matter-only simulations. In such simulations, the mass of a halo, $M_{\rm h}$, is the sum of the dark matter plus baryon mass. Therefore, when comparing to hydrodynamical simulations, we should not compare the dark matter halo mass to $M_{\rm h}$, but rather $\Omega_{\rm m}/\Omega_{\rm dm}$ times the dark matter mass (with, of course, $\Omega_{\rm m}$ and $\Omega_{\rm dm}$ the mean cosmological mass and dark matter density in units of the critical density, respectively). Of course in reality, outflows of baryons due to feedback from star formation slow the growth in mass of a halo (e.g. Sawala et al. 2015), a process we will neglect in this analytical investigation. We are now in a position to compute the CDDF and study its evolution.

2.2 The CDDF and its redshift evolution

Numerically integrating equation (15) yields the CDDF with the result plotted in panel (a) of Fig. 2 at four redshifts. The model (coloured curves for different redshifts) is compared to the results from a hydrodynamical simulation at $z = 3$ (yellow line connecting diamonds) from the OWLS project (Schaye et al. 2010), post-processed with radiative transfer using the URCHIN reverse ray-tracing code described by Altay & Theuns (2013), as presented by Altay et al. (2011). Also shown as yellow diamonds with error bars is the observed CDDF of DLAs at a mean redshift of $\langle z \rangle \approx 2.5$ as measured by Noterdaeme et al. (2012) from the SDSS DR9 (Ahn et al. 2012)), and the 'sub-DLAs' measured by Zafar et al. (2013) at $z \sim 3$ (yellow circles). Simulation and model are in excellent agreement with the data (better than 50 per cent) above the DLA threshold, $N_{\rm H\,I} > 10^{20.3}\,{\rm cm}^{-2}$. The model also agrees with the simulation at lower columns although not as well, with in particular the transition from mostly neutral absorbers (i.e. DLAs) to absorbers that are highly ionized in the model (sub-DLAs, $N_{\rm H\,I} \sim 10^{19-20.3}\,{\rm cm}^{-2}$ and LLSs, $N_{\rm H\,I} \geq 10^{17.2}\,{\rm cm}^{-2}$) more abrupt than in the simulation or in the data. However, the overall agreement at higher column densities between the simple model and the simulations, as plotted in the inset of Fig. 2(a), is encouraging. We note that the latter include molecule formation but the model does not (but see Section 2.5).

What determines the shape of the 'knee' feature at $N_{\rm H\,I} \sim 10^{20}\,{\rm cm}^{-2}$? As illustrated in Fig. 1, when the impact parameter b becomes smaller than $r_{\rm I}$, the radius of the ionization front, the column density rapidly increases by $\sim$2 orders of magnitude for a small change in b. For a *given* halo, this results in a nearly flat region in $g(N_{\rm H\,I}, M_{\rm h}) \propto \mathrm{d}\sigma/\mathrm{d}N_{\rm H\,I}$, as seen in panel (c) of Fig. 1: This is the origin of the knee. Zheng & Miralda-Escudé (2002) previously pointed out the connection between the rapid onset of self-shielding in a spherical cloud and the appearance of a knee in the CDDF; see also Petitjean, Bergeron & Puget (1992). With the CDDF, $f(N_{\rm H\,I})$, an integral over $g(N_{\rm H\,I}, M_{\rm h})$, the knee in g results in a knee in f; however, the shapes are different because the location of the knee is weakly dependent on $M_{\rm h}$. We will return to this after first investigating evolution.

The observed CDDF evolves very weakly even over the extreme redshift range $z = 0$–5. Such weak evolution is reproduced by simulations; see e.g. fig. 1 in Rahmati et al. (2013), although the underlying reason for the near-absence of evolution from $z = 2$–5 has not been discussed in great detail. The model also shows very weak evolution; see panel (a) of Fig. 2. Given the weak dependence of g on halo mass in the current model, weak evolution in f requires weak evolution in g.

We therefore examine the predicted evolution of the function $g(N_{\rm H\,I}, M_{\rm h}) \propto (\mathrm{d}\sigma/\mathrm{d}N_{\rm H\,I})\,(\mathrm{d}n/\mathrm{d}\log M_{\rm h})$ of equation (14) in more detail, starting from equation (13) for the evolution of the cross-section, $\mathrm{d}\sigma/\mathrm{d}N_{\rm H\,I}$. Using $\sigma = \pi b^2$, we solve equation (13) for the value of the impact parameter b for a sightline through a halo of mass $M_{\rm h}$ to have a given column density $N_{\rm H\,I}$. Keeping $M_{\rm h}$ and $N_{\rm H\,I}$ both constant, and neglecting the contribution from the integral I, the redshift dependence is due to the evolution of $n_{\rm H,0}$, the (total) hydrogen density at the edge of the halo, and $R_{\rm h}$, the virial radius of a halo of given mass $M_{\rm h}$. This yields for the net redshift dependence

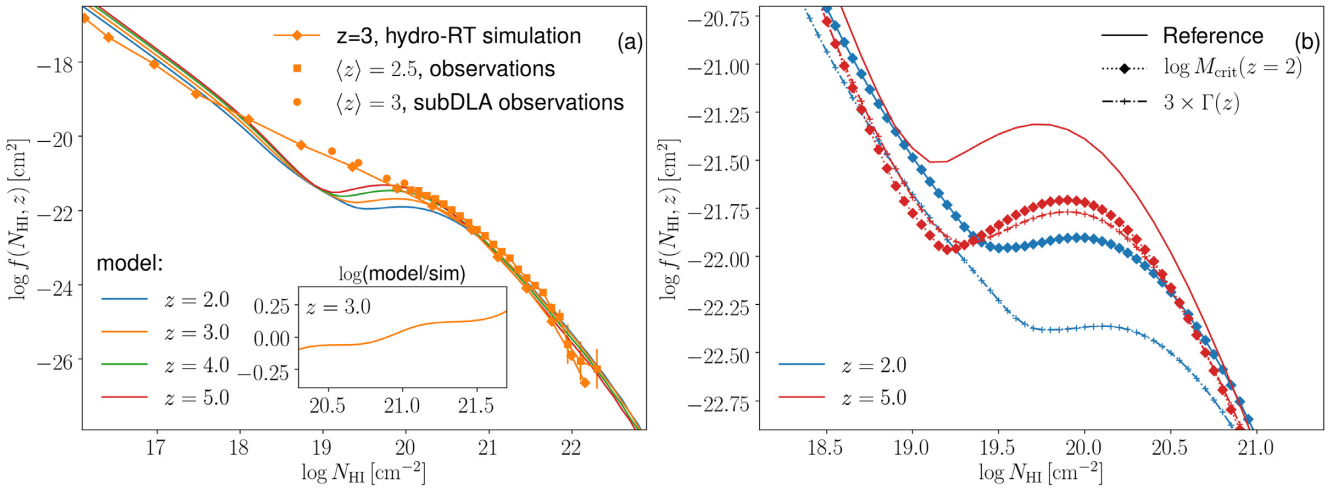

Figure 2. Panel (a): The model CDDF function $f(N_{\rm HI}, z)$, at various redshifts plotted in solid lines. Overplotted is $f(z = 3)$ for the OWL simulations (Schaye et al. 2010) presented by Altay et al. (2011) (yellow line connecting diamonds) and $f(\langle z\rangle = 2.5)$ for DLAs measured by Noterdaeme et al. (2012) (yellow squares) and sub-DLAs from Zafar et al. (2013) (yellow circles), which both fall approximately on top of the yellow simulations line. The inset shows the logarithm of the ratio of model over simulation at $z = 3$. Panel (b): $f(N_{\rm HI}, z)$ at $z = 2$ and 5 for the reference model (solid lines). A variation on the reference model in which the critical mass, $M_{\rm crit}$ (below which halo gas is photoevaporated and no longer contributes to f), does not evolve, $M_{\rm crit}(z) = M_{\rm crit}(z = 2)$, is shown as dotted lines connecting diamonds (this variation overlaps with the reference model at $z = 2$). Another variation in which the amplitude of the ionizing background, Γ, is multiplied by a factor of 3 at all z is shown as dot–dashed lines connecting crosses.

of σ and its derivative with respect to $N_{\rm HI}$

$$\frac{{\rm d}\sigma}{{\rm d}N_{\rm HI}} \propto n_{\rm H,0}^{2/(\alpha-1)}\, R_{\rm h}^{2\alpha/(\alpha-1)} \propto (1+z)^{6/(\alpha-1)}\,(1+z)^{-2\alpha/(\alpha-1)} \propto (1+z)^{2(3-\alpha)/(\alpha-1)}. \quad (16)$$

This scaling is a result of haloes becoming larger at later times, $R_{\rm h} \propto (1+z)^{-1}$, but less dense, $n_{\rm H,0} \propto (1+z)^3$. The density dependence is stronger and the cross-section (at a given column density and mass) *decreases* with time.

However, the (co-moving) number density of haloes with mass $M_{\rm h}$, ${\rm d}n/{\rm dlog}\,M_{\rm h}$, *increases* with time. In the Press–Schechter approximation, the increase is proportional to the linear growth rate, $D(z)$, which to a good approximation is $D(z) \approx 1/(1+z)$ in the redshift range $z = 2$–5. However, in the mass range of interest, $9 \le \log M_{\rm h}/{\rm M}_\odot \le 13$, the evolution is slightly stronger, more like ${\rm d}n/{\rm dlog}\,M_{\rm h} \propto (1+z)^{-1.7}$.

The opposite evolution of the cross-section and the number density of haloes yields for the net evolution for the contribution of haloes with given $M_{\rm h}$ to the CDDF at a given (self-shielded) column density,

$$g(N_{\rm HI}, z) \propto \frac{{\rm d}n}{{\rm d}\log M_{\rm h}}\frac{{\rm d}\sigma}{{\rm d}N_{\rm HI}} \propto (1+z)^{-1.7}\,(1+z)^{2(3-\alpha)/(\alpha-1)} \approx (1+z)^{-0.4}. \quad (17)$$

Using the value at $z = 3$ as a pivot point, $g(z = 2)/g(z = 3) \approx 1.1$, and $g(z = 5)/g(z = 3) \approx 0.86$. Therefore, as time progresses, more haloes of a given mass $M_{\rm h}$ appear at lower z but the cross-section of individual haloes decreases. These two factors nearly compensate each other, resulting in weak evolution of the function g – and explaining the weak evolution in the column-density distribution of DLAs, $f(N_{\rm HI})$.

These analytical estimates are tested in more detail in Fig. 3. In panel (a) of that figure, we show the evolution of the cross-section, ${\rm d}\sigma/{\rm d}N_{\rm HI}$ for haloes with various masses (coloured lines), and for column densities of $\log N_{\rm HI}[{\rm cm}^{-2}] = 19.3$ (dotted), 20.3 (solid), and 21.3 (dashed lines). Evolution is relatively weak, following approximately the evolution ${\rm d}\sigma/{\rm d}N_{\rm HI} \propto (1+z)^{2(3-\alpha)/(\alpha-1)}$ shown as the dot–dashed cyan line, for all $M_{\rm h}$ and values of $N_{\rm HI}$ shown. In panel (b), we show the evolution of the co-moving number density, ${\rm d}n/{\rm dlog}\,M_{\rm h}$, computed using COLOSSUS (Diemer 2018). To guide the eye, we overplot as the dot–dashed cyan line, the scaling $\propto(1+z)^{-1.7}$, which captures at least approximately the evolution of the lower mass haloes, underestimating the evolution for $\log M_{\rm h}/{\rm M}_\odot = 12$. Finally, in panel (c) we plot the evolution of the contribution of haloes of given mass and column density, $g(N_{\rm HI}, M_{\rm h})$. Given that the trends in cross-section and number density are weak and in the opposite direction, the evolution in g is even weaker, following reasonable well the trend $\propto(1+z)^{-0.4}$ predicted earlier for self-shielded column-density systems, and shown as the dot–dashed cyan line.

It is also worth exploring the evolution of the covering factor, the ratio $\sigma/(\pi R_{\rm h}^2)$, which follows from equation (13) and is plotted in Fig. 4. The DLA cross-section (in proper kpc^2) increases slowly with redshift at constant halo mass $M_{\rm h}$, and is approximately $\propto M_{\rm h}$, as can be seen in the upper panel. Because the virial radius decreases with z, the covering factor increases faster with z than the cross-section (lower panel). The values of the covering factor and their evolution are in very good agreement with those computed by Rahmati et al. (2015) for galaxies in the EAGLE simulation (Schaye et al. 2015) with $M_{\rm h} \ge 10^{12}\,{\rm M}_\odot$ (filled red diamonds). Another comparison is with the high-resolution simulations of Faucher-Giguère & Kereš (2011) that yield a covering factor of $\sigma_{\rm DLA}/(\pi R_{\rm h}^2)$ of an ∼3–10 per cent for $M_{\rm h} \sim$ (2–3) $\times\, 10^{11}\,{\rm M}_\odot$ at $z = 2$ – values comparable to what we find here.[8]

[8]The simulations by Faucher-Giguère et al. (2015) that include feedback are claimed to give a far higher covering factor of 0.2–0.4 for such haloes.

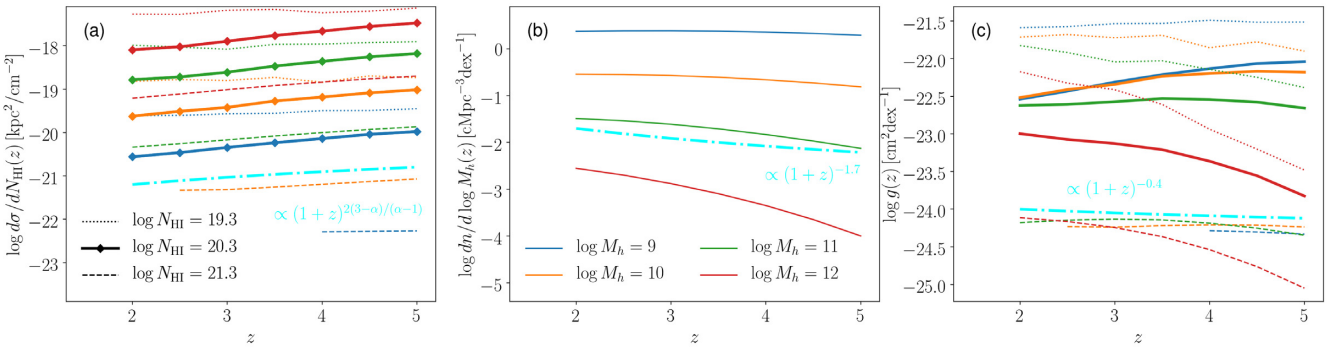

Figure 3. Dependence of the contribution of haloes with given mass ($\log M_{\rm h}/{\rm M}_\odot = 9$, 10, 11, and 12 shown in red, green, yellow, and blue, respectively) at a given column density ($\log N_{\rm H\,I}/{\rm cm}^{-2} = 19.3$, 20.3, and 21.3 as dotted, thick solid, and dashed, respectively) to the CDDF as a function of redshift, from equation (10). Panel (a): cross-section, $\mathrm{d}\sigma/\mathrm{d}N_{\rm H\,I}$, as a function of z. Panel (b): dark matter halo number density, $\mathrm{d}n/\mathrm{dlog}\,M_{\rm h}$, as a function of redshift. Panel (c): net contribution $g(N_{\rm H\,I}, M_{\rm h}, z)$ of haloes of mass $M_{\rm h}$ to the CDDF as column density $N_{\rm H\,I}$, as a function of redshift. Cyan dash–dotted lines in each panel indicate the redshift scaling as annotated. Panels (a) and (b) show that the evolution of cross-section and number density is relatively weak, as expected (see the text). The trends are also in the opposite direction, leading to even weaker evolution of g, as shown in panel (c).

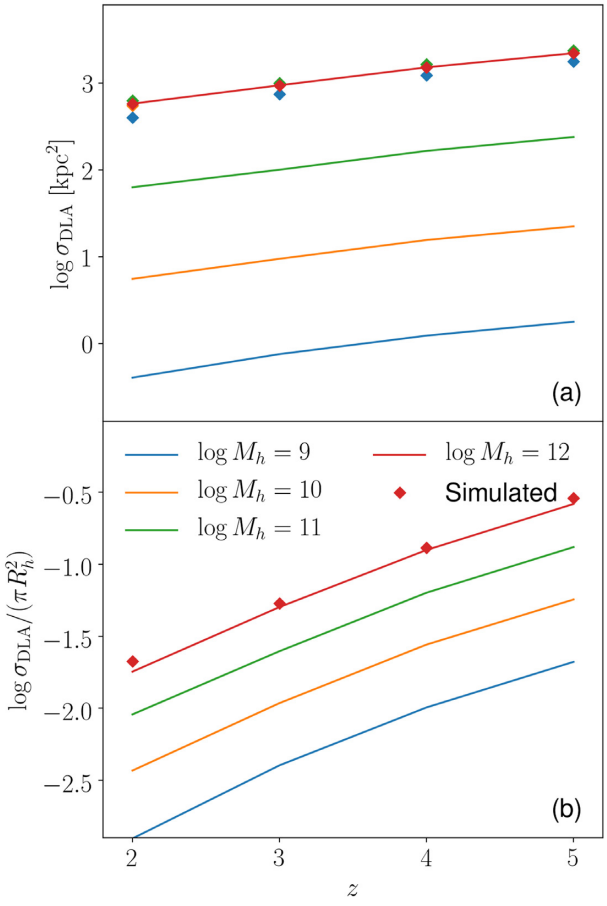

Figure 4. Panel (a): Coloured curves are the model's DLA cross-section, $\sigma_{\rm DLA}$, in proper units, as a function of redshift. Curves are coloured according to halo mass, as per the legend in panel (b). Filled diamonds show $\sigma_{\rm DLA}$ scaled by $10^{12}\,{\rm M}_\odot/M_{\rm h}$. Panel (b): DLA covering fraction, $\sigma_{\rm DLA}/(\pi R_{\rm h}^2)$, as a function of redshift for haloes of different masses (colours). The filled red diamonds are the covering factors computed using the fitting formula presented by Rahmati et al. (2015) from the EAGLE simulations, for haloes with masses $\geq 10^{12}\,{\rm M}_\odot$.

According to equation (13), $\sigma \propto R_{\rm h}^{2\alpha/(\alpha-1)} \propto M_{\rm h}^{2\alpha/(3(\alpha-1))} \approx M_{\rm h}^{1.22}$. We have multiplied the values of σ for each halo by $(10^{12}\,{\rm M}_\odot/M_{\rm h})^{1.22}$ and overplotted them on Fig. 4 as filled diamonds. The fact that these symbols fall nearly on top of the $M_{\rm h} = 10^{12}\,{\rm M}_\odot$ values demonstrates that this scaling works very well. The value of the exponent $\beta \sim 1.22$ in $\sigma \propto M_{\rm h}^{\beta}$ is a bit larger than that found in the numerical simulations presented by Bird et al. (2014) (who find that $\beta < 1$ depending on the feedback strength in their simulations) and more comparable to that inferred from the observed DLA bias by Font-Ribera et al. (2012) and Pérez-Ràfols et al. (2018), who prefer $\beta \sim 1.1$. With $\beta = 1.22$, the DLA *covering factor* scales as $\sigma/R_{\rm h}^2 \propto M_{\rm h}^{0.56}$ in our model.

Two other trends are worth noting in panel (c) of Fig. 3. First, at high column densities ($\log N_{\rm H\,I}\,[{\rm cm}^{-2}] = 21.3$), haloes of $\log M_{\rm h}/{\rm M}_\odot = 10$–12 contribute about equally to g (see the dashed lines). As discussed before, the dependence of g on $N_{\rm H\,I}$ is weak at high column; see equation (14). Secondly, the dependence becomes stronger at lower columns, with lower mass haloes contributing significantly more particularly at higher z (contrast the dotted and solid lines).

The second observation brings us back to the shape of the knee in $f(N_{\rm H\,I})$. At higher z, lower mass haloes contribute relatively more to $f(N_{\rm H\,I})$ per decade in halo mass. In addition, the value of $M_{\rm crit}$ – the halo mass below which gas is evaporated from haloes by photoheating by the ionizing background – is lower at higher z, meaning that lower mass haloes contribute even more to f at $z = 5$ compared to $z = 2$. The result is a noticeable increase in the number density of absorbers slightly below the DLA threshold moving the location of the knee to lower column densities: This increase is due to an increase in the contribution of lower mass haloes. The consequence of this is best appreciated by comparing $f(N_{\rm H\,I}, z)$ at $z = 5$ (red lines) versus at $z = 2$ (blue line) in panel (a) of Fig. 2: There are considerably more sub-DLAs (with $N_{\rm H\,I}$ slightly below $10^{20.3}\,{\rm cm}^{-2}$) at $z = 5$ compared with $z = 2$. Such a change in shape is also apparent in simulations (see e.g. fig. 1 in Rahmati et al. 2015; see also Sykes et al., in preparation). The data also suggest an increased abundance of sub-DLAs with increasing z (Zafar et al. 2013).

To illustrate the impact of $M_{\rm crit}$ on the shape of the knee, we plot in panel (b) of Fig. 2 the CDDF, $f(N_{\rm H\,I}, z)$, for $z = 2$ and 5, comparing the default model in which $M_{\rm crit}$ evolves (solid lines) with a variation in which the critical mass is kept fixed at its value at $z = 2$ (dotted lines connecting diamonds). These models obviously fall

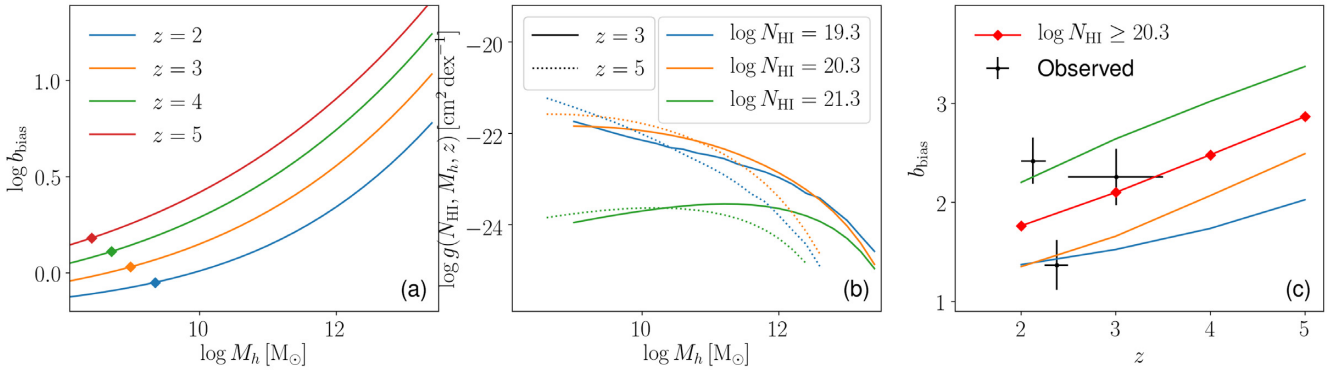

Figure 5. Evolution of DLA bias. Panel (a): halo bias as a function of mass at different redshifts (various colours), computed for the Planck Collaboration XVI (2014) cosmology using the COLOSSUS code of Diemer (2018) with the Tinker et al. (2010) prescription. The solid diamonds indicate the critical mass, $M_{\rm crit}$, below which gas in haloes is photoevaporated according to the simulations of Okamoto et al. (2008). Haloes of lower mass are assumed not to contribute to the CDDF. Panel (b): differential contribution of haloes of a given mass to the CDDF from equation (14) for three values of $N_{\rm H\,I}$ (different colours) and two redshifts (different line styles) as per the legend. Notice in particular that g depends weakly on halo mass over a large range in $M_{\rm h}$. Panel (c): bias of absorbers at a given value of the column density, as per the legend in panel (b); the red line corresponds to DLAs. The black squares are the observed DLA bias measurements from Pérez-Ràfols et al. (2018).

on top of each other at $z = 2$, but the shape of the knee for the $z = 5$ curves changes significantly – resulting in a large decrease in the number density of sub-DLAs. The panel also shows another model variation, in which $M_{\rm crit}$ evolves as before, but the amplitude Γ of the ionizing background is multiplied by a factor of 3 at all z above its value in the default model (that of Haardt & Madau (2012); this variation is shown as dot–dashed line connecting crosses). Increasing Γ changes the shape of the knee in a similar way as increasing $M_{\rm crit}$, but the two variations do change the shape of the CDDF differently at lower column densities. If it were possible to constrain Γ robustly by observations at lower columns, for example in the Lyman-α forest (e.g. Becker & Bolton 2013), then evolution of the shape of the knee could be used to test models for the evolution of $M_{\rm crit}$. In fact, it is likely easier to constrain robustly the *evolution* of Γ rather than its amplitude at any z – this might be enough to test whether $M_{\rm crit}$ evolves as expected. Other effects may also play a role in shaping the knee, for example the temperature of the absorbing gas (McQuinn, Oh & Faucher-Giguère 2011) or the hardness of the ionizing radiation that will affect the width of the ionization front. Finally, we note the relatively substantial effect of the value of $M_{\rm crit}$ on the number density of LLSs (see also Fumagalli et al. 2013).

Armed with an estimate of how much haloes of given mass contribute to the CDDF, it is now straightforward to compute the bias of DLAs, to which we turn next.

2.3 DLA bias

The term *bias* was famously coined by Davis et al. (1985) to describe the fact that observed galaxies are more strongly clustered than the mass seen in numerical simulations, with Kaiser (1984) showing that such biasing naturally follows from the assumption that galaxies form at local maxima in a Gaussian density field. Mathematically, the bias factor[9] $b_{\rm bias}$ of a population of objects – for example, haloes with a given mass – can be defined as the ratio of their power spectrum, $P(M_{\rm h}, z)$, to that of the mass, $P_{\rm m}$: $b^2_{\rm bias}(M_{\rm h}, z) \equiv P(M_{\rm h}, z)/P_{\rm m}(z)$. The COLOSSUS tool of Diemer (2018) implements several methods for estimating $b_{\rm bias}$ for haloes of a given mass at a given redshift. Below we use Diemer (2018)'s implementation of the model by Tinker et al. (2010). Given the function $g(N_{\rm H\,I}, M_{\rm h}, z)$ and this bias function $b_{\rm bias}(M_{\rm h}, z)$, we compute the bias of lines with a given value of the column density as (see also Padmanabhan et al. 2016)

$$b_{\rm bias}(N_{\rm H\,I}, z) = \frac{\int_{\log M_{\rm crit}(z)}^{\infty} {\rm d}\log M_{\rm h}\ \{b(M_{\rm h}, z) \times g(N_{\rm H\,I}, M_{\rm h}, z)\}}{\int_{\log M_{\rm crit}(z)}^{\infty} {\rm d}\log M_{\rm h}\ \{g(N_{\rm H\,I}, M_{\rm h}, z)\}}, \tag{18}$$

and the bias of DLAs as

$$b_{\rm bias}({\rm DLA}, z) = \frac{\int_{20.3}^{\infty} {\rm d}\log N_{\rm H\,I} \int_{\log M_{\rm crit}(z)}^{\infty} {\rm d}\log M_{\rm h}\, \mathcal{F}_1(M_{\rm h}, N_{\rm H\,I}, z)}{\int_{20.3}^{\infty} {\rm d}\log N_{\rm H\,I} \int_{\log M_{\rm crit}(z)}^{\infty} {\rm d}\log M_{\rm h}\, \mathcal{F}_2(M_{\rm h}, N_{\rm H\,I}, z)},$$

$$\mathcal{F}_1(M_{\rm h}, N_{\rm H\,I}, z) = b(M_{\rm h}, z) \times N_{\rm H\,I} \times g(N_{\rm H\,I}, M_{\rm h}, z)$$

$$\mathcal{F}_2(M_{\rm h}, N_{\rm H\,I}, z) = N_{\rm H\,I} \times g(N_{\rm H\,I}, M_{\rm h}, z). \tag{19}$$

The results are illustrated in Fig. 5. In panel (a), we plot the bias function $b_{\rm bias}(M_{\rm h}, z)$ computed using COLOSSUS (Diemer 2018). Superposed as filled diamonds are the values of the critical mass, $M_{\rm crit}$, computed from Okamoto et al. (2008) for reference. In panel (b), we plot the function $g(N_{\rm H\,I}, M_{\rm h}, z)$ for three values of $N_{\rm H\,I}$ (colours). As we noted and explained before, the function g depends relatively weakly on $M_{\rm h}$ over a large range in halo mass. In our model, it falls abruptly to zero for haloes with mass $M_{\rm h} < M_{\rm crit}$, by construction, and at high mass decreases exponentially due to the exponential cut-off in the halo mass function. A comparison between the solid and dotted lines, which correspond to redshifts $z = 3$ and 5, respectively, shows how the function g evolves. $M_{\rm crit}$ decreases with increasing z – so that lower mass haloes contribute more to g at higher z. Additionally, the location of the exponential cut-off in the mass function also decreases with increasing z and consequently the relative contribution of lower mass haloes to the CDDF increases with z.

Combining panels (a) and (b) yields the bias of absorbers, plotted in panel (c). In addition to the bias of the absorbers shown in panels (a) and (b), we also plot the bias of DLAs (red line connecting solid diamonds). The bias increases with z for all column densities shown in the panel. So, even though there is a tendency for lower mass haloes to increase their contribution to the cross-section with increasing redshift (which would decrease $b_{\rm bias}$), the bias of such

[9]We use the symbol $b_{\rm bias}$ to denote the bias factor to avoid confusion with the impact parameter, b.

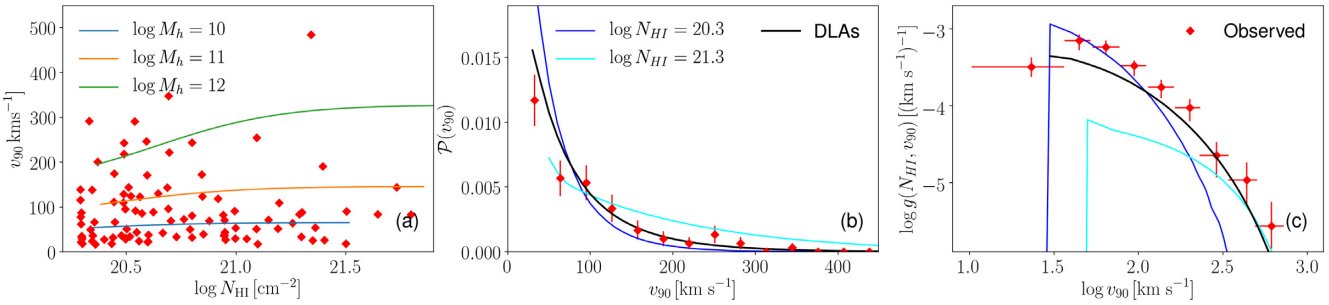

Figure 6. DLA line width, v_{90}, at redshift $z = 3$. Panel (a): v_{90} versus column density, $N_{\rm H\,I}$. Lines are the model prediction, with different colours referring to different halo masses, $M_{\rm h}$ in solar masses, as indicated in the legend. Along a curve for a given halo mass, impact parameter decreases with increasing $N_{\rm H\,I}$. Red squares are the observations by Neeleman et al. (2013). Panel (b): Fraction of DLAs with a given line width. Lines are the model prediction, with blue and cyan lines for column densities of log $N_{\rm H\,I}$[cm^{-2}] = 20.3 and 21.3, respectively, and the thick black line the model prediction for DLAs, log $N_{\rm H\,I}$[cm^{-2}] > 20.3. Red symbols correspond to the data of Neeleman et al. (2013) as in panel (a), plotted with Poisson error bars. Each histogram is normalized to unity. Panel (c): Number density of absorbers with a given line width. Lines are the model prediction from equation (23), with the same colouring as in panel (b). Red symbols with error bars are the data from Prochaska et al. (2003) as plotted in fig. 9 of Pontzen et al. (2008), for DLAs in the redshift interval [1.6, 4.5].

haloes *increases* even more rapidly with z, leading to a net increase in $b_{\rm bias}$. We also note that the bias increases with column density, which is not surprising, but at $z \sim 2$, the bias is approximately the same for log $N_{\rm H\,I}$ [cm^{-2}] = 19.3 and 20.3 (blue and orange lines, respectively). Since bias increases with column density, the bias of DLAs $b_{\rm bias}$(DLA) > $b_{\rm bias}$(log $N_{\rm H\,I}$ [cm^{-2}] = 20.3). For reference, we overplot the bias measurements of DLAs from Pérez-Ràfols et al. (2018) as *black symbols with error bars*.[10] Although the agreement is not perfect, our DLA model yields reasonably high values of $b_{\rm bias}$, even though low-mass haloes contribute significantly.

2.4 DLA line widths

To measure the velocity extent of DLAs expected in the model, we consider sightlines that intersect neutral gas. In the current model, those have impact parameter $b \leq r_{\rm I}$, the radius of the ionization front. We further assume that the gas is flowing radially with hydrogen accretion rate

$$\dot{M}_{\rm H} = \omega_{\rm b}\, X\, \dot{M}_{\rm h}, \tag{20}$$

where we use equation (1) for the profile and equation (2) for the halo accretion rate. Using the continuity equation then yields for the radial inflow velocity of the hydrogen gas

$$\begin{aligned} v_r &= \frac{\dot{M}_{\rm H}}{4\,\pi r^2\, m_{\rm H}\, n_{\rm H}(r)} \\ &= \frac{1+z}{10\,\Omega_{\rm m}} \left(b - \frac{a}{1+z}\right) \left(\frac{r}{R_{\rm h}}\right)^{\alpha-2} v_{\rm h} \\ &\approx 210\,{\rm km\,s^{-1}} \left(\frac{M_{\rm h}}{10^{12}\,{\rm M_\odot}}\right)^{1/3} \left(\frac{1+z}{4}\right)^{3/2} \left(\frac{r}{R_{\rm h}}\right)^{\alpha-2}, \end{aligned} \tag{21}$$

where the numerical values use the Planck Collaboration XVI (2014) values of the cosmological parameters. This infall velocity depends little on radius in the cases we are interested, i.e. when the slope of the density profile $\alpha \approx 2$. The component of the velocity along the line of sight is $v_z = \cos(\theta)\, v_r$, where $\cos(\theta) = z/r$ depends on the distance r to the centre and on $z = (r^2 - b^2)^{1/2}$. Given that v_r only depends weakly on r means that absorption in neutral gas occurs over a velocity range of approximately $[-v_{\rm H\,I}, v_{\rm H\,I}]$, where $v_{\rm H\,I} = (1 - b^2/r_{\rm I}^2)^{1/2}\, v_r(r = r_I)$, where $v_r(r = r_{\rm I})$ is the value of the infall velocity at the location $r_{\rm I}$ of the ionization front.

Observationally, the line width associated with a DLA is quantified by a velocity called v_{90}, defined such that 90 per cent of the optical depth of a line associated with a metal transition occurring in neutral gas is enclosed by this velocity interval. To connect this to our velocity profile, we will identify v_{90} with 2 $v_{\rm H\,I}$,

$$v_{90} = 2 v_r(r_{\rm I}) \left(1 - \frac{b^2}{r_{\rm I}^2}\right)^{1/2}, \tag{22}$$

which is thus the velocity extent[11] of neutral gas at impact parameter b for a halo of given mass, $M_{\rm h}$. As we will show below, there is a (relatively weak) dependence of v_{90} on column density for any given halo, since at low columns the sightline grazes the ionization front at $r = r_{\rm I}$ and gas flows mostly perpendicular to the sightline, yielding a low value of v_{90}. At low b, the column density is near maximum, gas flows along the sightline, and hence $v_{\rm H\,I}$ is maximal. This geometric dependence does not translate directly into a correlation between $N_{\rm H\,I}$ and v_{90} *for a population* of DLAs, as we show below.

We obtain the joint probability distribution function for lines to have a given value of column density and v_{90} starting from equation (22), by changing variables from b to $N_{\rm H\,I}$ using equation (12), eliminating $r_{\rm I}$ using equation (8), and finally using equation (10):

$$g(N_{\rm H\,I}, v_{90}) \equiv \frac{\partial^3 N}{\partial X \partial N_{\rm H\,I} \partial v_{90}} = g(M_{\rm h}, N_{\rm H\,I}) \left(\frac{{\rm d}v_{90}}{{\rm d}\log M_{\rm h}}\right)^{-1}. \tag{23}$$

Integrating this quantity over $N_{\rm H\,I}$, for log $N_{\rm H\,I}$[cm^{-2}] $\geq$ 20.3, yields the line width distribution for DLAs. It turns out that not surprisingly most of the dependence of v_{90} on halo mass arises from its dependence on the halo's virial velocity, so that approximately dlog v_{90}/dlog $M_{\rm h} \approx$ dlog $v_{\rm h}$/dlog $M_{\rm h} = 1/3$ and hence dv_{90}/dlog $M_{\rm h} \propto v_{90}$. Results are shown in Fig. 6, where model results are shown at $z = 3$.

In panel (a) of Fig. 6, we plot as coloured lines the relation between v_{90} and the column density for various values of the halo mass; $M_{\rm h}$, in units of M$_\odot$, can be read from the legend. The more massive the halo, the higher v_{90} at a given value of $N_{\rm H\,I}$, reflecting the $v_{90} \propto v_{\rm h}$ dependence. The impact parameter decreases with increasing $N_{\rm H\,I}$

[10] These correspond to the red filled circles in fig. 4 of that paper.

[11] With the factor 2 accounting for the gas falling away from as well as well as towards the observer.

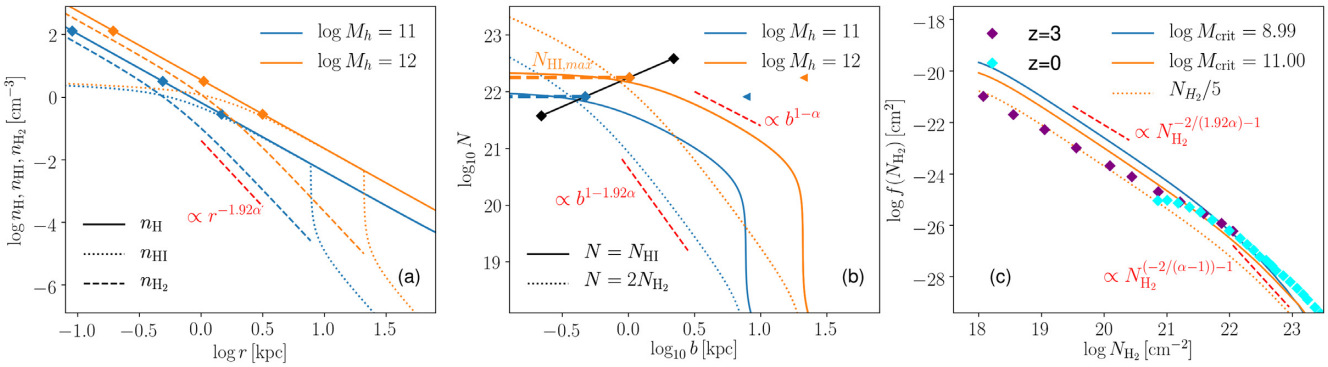

Figure 7. Molecular hydrogen in haloes at redshift $z = 3$. Panel (a): Assumed radial distribution of the total hydrogen density (n_H, solid line), the atomic hydrogen density (n_{HI}, dotted line), and the molecular hydrogen density (n_{H_2}, dashed line) in haloes with mass $M_h = 10^{11}$ and 10^{12} M$_\odot$ (blue and orange lines, respectively); the power-law exponent is $\alpha = 2.2$. The n_H and n_{HI} distributions are repeated from Fig. 1, except that now we subtract $2 \times n_{H_2}$ that causes the downturn in the n_{HI} density at small radii. When the molecular fraction is low, n_{H_2} is approximately proportional to $n_H^{1.92}$, with the factor 0.92 the exponent appearing in equation (24). This scaling is indicated by the red dashed line. At higher densities, the molecular fraction tends to unity so that $2n_{H_2} \approx n_H$. The left and rightmost filled diamonds correspond to the maximum and minimum densities for which Blitz & Rosolowsky (2006) measured the fitting relation of equation (24); the middle filled diamond corresponds to the density where $R_{mol} = 1$. Panel (b): Corresponding column densities of atomic gas (solid line) and molecular gas (dotted lines) as a function of impact parameter, b. The slopes for pure power-law profiles are plotted as red dashed lines. When $N_{HI} \gtrapprox 10^{22}$ cm^{-2}, gas in the model becomes increasingly molecular, with the transition column dependent on halo mass. The thick horizontal dashed lines show the maximum H I column density as computed from equation (26), with the diamonds at the location where $b = r_{H_2}$, the radius within which $R_{mol} > 1$. The black line shows the relation r_{H_2}–$N_{HI,max}$, with further black diamonds indicating halo masses of log M_h[M$_\odot$] = 10 and 13. The left pointing triangles show the location of the ionization front, plotted at $b = R_I$. Panel (c): Corresponding molecular hydrogen CDDF. The blue and orange lines are the model prediction when summing over all haloes more massive than $10^{8.99}$ and 10^{11} M$_\odot$, respectively. At column $N_{H_2} \lessapprox 10^{22}$ cm^{-2}, gas is mostly atomic and the H_2 CDDF is a power law with a slope $f(N_{H_2}) \propto N_{H_2}^{-2/(1.92\alpha)}$, indicated by the upper red dashed line. At higher column densities, gas becomes mostly molecular, and the CDDF steepens to $f(N_{H_2}) \propto N_{H_2}^{-2/(\alpha-1)}$ – the same slope as the N_{HI} CDDF at high column density – indicated by the lower red dashed line. These (approximate) power-law dependences result from the dependence of cross-section on column density (see the text). The purple diamonds depict the observed CDDF for molecular hydrogen at $z \approx 3$ reported by Balashev & Noterdaeme (2018), and the cyan crosses are the $z = 0$ data from Zwaan & Prochaska (2006). The orange dotted line assumes that the molecular abundances is 5 times lower than that predicted by equation (24).

for a given value of M_h; as explained, this increases v_{90} as gas flows increasingly along the line of sight. For reference, we show as red symbols the data of Neeleman et al. (2013). Panel (b) shows the fraction of DLAs with a given value of v_{90} as a black thick line, as well as the line width distribution for two values of the column density, log N_{HI}[cm^{-2}] = 20.3 (dark blue) and 21.3 (cyan). This reveals a weak trend for lower column density DLAs to have lower values of v_{90}. Shown as red symbols are the histogrammed data of Neeleman et al. (2013), showing that the model gives a reasonable distribution of velocity widths. In panel (c), we plot the number of lines with a given value of v_{90} from equation (23), for the same cuts in column density as in panel (b). Overplotted as red symbols is the observed distribution for DLAs from Prochaska et al. (2003), which should be compared to the black line.

The model is in reasonable agreement with the data, producing a small number of quite broad lines with $v_{90} > 400$ km s^{-1}, and a large number of narrow lines with a rather abrupt cut-off at $v_{90} \lessapprox 25$ km s^{-1}, as observed. Comparing panels (b) and (c), it seems that the model slightly undershoots the number of narrow-lined DLAs when compared to the Prochaska et al. (2003) data, whereas it overshoots the number of narrow-lined DLAs when compared to the Neeleman et al. (2013) data. Either this means that the two data sets are not quite consistent, possibly just due to the small number statistics, or it may point to redshift evolution in the data.

2.5 Molecules

Since at least some fraction of DLAs correspond to a sightline puncturing a galaxy, some DLA sightline should also intersect molecular gas. Here, we try to estimate how often this occurs. To do so, we use the simple empirical pressure–H_2/H I relation from Blitz & Rosolowsky (2006).

Measuring the surface density of local spiral galaxies in both neutral gas and molecular gas, Blitz & Rosolowsky (2006) found that the ratio of these surface densities scaled with central gas pressure (p) approximately as (their equation 12)

$$R_{mol} \equiv \frac{\Sigma(H_2)}{\Sigma(H\,I)} = \left(\frac{p/k_B}{3.5 \times 10^4\,\mathrm{K\,cm^{-3}}} \right)^{0.92}, \qquad (24)$$

where k_B is Boltzmann's constant. In their paper, Blitz & Rosolowsky (2006) verify this relation in the range $3 \times 10^3 \le (p/k_B)/(\mathrm{K\ cm^{-3}}) \le 2 \times 10^6$. We will use this fit to relate the volume densities of molecular and atomic hydrogen inside the ionization front, setting

$$\frac{2\,n_{H_2}}{n_H} \approx \left(1 + \frac{1}{2R_{mol}} \right)^{-1}. \qquad (25)$$

Given the assumed hydrogen density profile in haloes, $n_H \propto r^{-\alpha}$, and setting the gas temperature to $T = 10^4$ K, we compute the gas pressure p, and substitute this value in the previous two relations to compute the molecular hydrogen density, n_{H_2}. Combining this with the number density of haloes with a given mass allows us to compute the H_2 CDDF. The results are illustrated in Fig. 7.

The left-hand panel repeats the (total) hydrogen profile, $n_H \propto r^{-\alpha}$, with $\alpha = 2.2$, from equation (1), replacing the atomic hydrogen density $n_{HI} \to n_{HI} - 2\,n_{H_2}$ to account for molecular gas. The profiles are shown for two halo masses and apply to redshift $z = 3$. The inclusion of molecules flattens the atomic profile towards the centre. When $R_{mol} \ll 1$ in self-shielded gas, $n_{H_2} \approx R_{mol}\,n_H \approx n_H^{1.92}$, since the gas pressure $p \propto n_H$ when gas is isothermal. Therefore, $n_{H_2} \propto r^{-1.92\alpha}$ in the outskirts of the halo, shown in the panel as the red dashed line.

At smaller radii, gas becomes mostly molecular so that $2n_{\rm H_2} \rightarrow n_{\rm H}$. The central diamond corresponds to the location where $R_{\rm mol} = 1$, with the outer and inner diamonds enclosing the region to which Blitz & Rosolowsky (2006) fitted equation (24). As could have been anticipated, gas in the central regions is mostly molecular, in a shell around that it is mostly neutral, and in the outskirts it is highly ionized. Another point to take away from this is that there is a large range at low values of $n_{\rm H_2}$ in the neutral shell of gas where relation equation (24) is *extrapolated*: We should therefore treat the predicted values of the molecular gas fraction at these lower densities with caution.

The middle panel of Fig. 7 shows the corresponding column density as a function of impact parameter, b, computed as in equation (5). As explained when discussing equation (6), if the radial density profile is a power law in radius, $\propto r^{-\beta}$, the column density is approximately a power law in impact parameter, $\propto b^{1-\beta}$. Using the values of β from the left-hand panel, we show the predicted power-law slopes as dashed red lines, for both the molecular and atomic column densities. The power-law approximations fit the curves well over a large range in impact parameter.

Comparing the $N_{\rm H\,I}$ profile with that in Fig. 1 shows that, not surprisingly, including molecules decreases the H I column density at small impact parameter, leading to a plateau in $N_{\rm H\,I}$ value at low b. The height of the plateau increases with halo mass, $M_{\rm h}$. We can estimate the approximate value of this maximum column density at $b = 0$ by assuming that gas in the spherical shell $r_{\rm H_2} \leq r \leq r_{\rm I}$ is neutral, gas at $r > r_{\rm I}$ is fully ionized, and gas at $r < r_{\rm H_2}$ is fully molecular. Here, $r_{\rm I}$ is the radius of the ionization front from equation (8), and $r_{\rm H_2}$ is the radius within which the gas is mostly molecular. For the latter, we use the value of the radius where $R_{\rm mol} = 1$, as in the left-hand panel. The maximum column density is then

$$N_{\rm H\,I,max} \approx 2 \int_{r_{\rm H_2}}^{r_{\rm I}} n_{\rm H}(r)\,{\rm d}r = 2\frac{n_{\rm H,0}\,R_{\rm h}}{\alpha-1}\left[\left(\frac{n_{\rm H_2}}{n_{\rm H,0}}\right)^{(\alpha-1)/\alpha} - \left(\frac{R_{\rm h}}{r_{\rm I}}\right)^{\alpha-1}\right], \quad (26)$$

which indeed increases with increasing $R_{\rm h}$ and hence $M_{\rm h}$. The corresponding values are plotted in the middle of Fig. 7 as the horizontal dashed lines, for both values of $M_{\rm h}$; they capture the numerical result quite accurately. The factor of 2 in equation (26) accounts for the sightline crossing the neutral shell twice.

We also plot the values of $(b = r_{\rm H_2}, N_{\rm H\,I,max})$ for halo masses $\log M_{\rm h}[{\rm M}_\odot] = 10$ and 13 in black, and for $\log M_{\rm h}[{\rm M}_\odot] = 11$ and 12 in blue and orange, respectively. For the last two values of $M_{\rm h}$, we also plot the point $(b = r_{\rm I}, N_{\rm H\,I,\,max})$ as left pointing triangles. Comparing the triangles and diamonds, it is clear that for decreasing b, when $b \leq r_{\rm I}$, the H I column density increases rapidly as gas becomes mostly neutral, and once $b \leq r_{\rm H_2}$, there is a kink in the H I column density–b relation, because the gas interior to $r_{\rm H_2}$ is mostly molecular.

Given the run of the molecular column density as a function of b and $M_{\rm h}$, we now sum over all haloes to compute the molecular hydrogen CDDF, shown in the right-hand panel of Fig. 7 at $z = 3$. The blue curve sums the contribution of all haloes with $M_{\rm h} > M_{\rm h,\,crit}$ – the critical halo mass below which haloes lose gas due to reionization – as we did for the H I CDDF. The slope of the CDDF is once more set by the dependence of the H_2 cross-section on impact parameter, just as we found for the H I CDDF. Given the power laws from the middle panel, this predicts approximately scalings of $f(N_{\rm H_2}) \propto N_{\rm H_2}^{(-2/(1.92\alpha)-1)} \approx N_{\rm H_2}^{-1.47}$ at low columns, $N_{\rm H_2} \lessapprox 10^{22}\,{\rm cm}^{-2}$, and $\propto N_{\rm H_2}^{-2.66}$ above that. The steepening at high column density is caused by the fact that these absorbers are mostly molecular, so that $2n_{\rm H_2} = n_{\rm H}$. For comparison, we overplot the observed CDDF at $z = 3$ from Balashev & Noterdaeme (2018), for which the slope at the lower column densities is slightly flatter at -1.29. We also overplot the CDDF at $z = 0$ from Zwaan & Prochaska (2006).

There is no obvious reason for the $z = 0$ data to smoothly fit on to the $z = 3$ data – although, as Balashev & Noterdaeme (2018) point out, in fact they do. At high columns, $N_{\rm H_2} \gtrapprox 10^{22}\,{\rm cm}^{-2}$, our default model (blue curve) reproduces the $z = 3$ data well, and fits smoothly on to the $z = 0$ data. However, below $N_{\rm H_2} \lessapprox 10^{21}\,{\rm cm}^{-2}$, the model increasingly overestimates the CDDF, although the observed and simulated slopes of the CDDFs are quite similar. Recalling our discussion of panel (a), we have extrapolated equation (24) to values much lower than those measured in the paper by Blitz & Rosolowsky (2006). It is these low densities and large impact parameters that cause the overestimate in the CDDF at columns $N_{\rm H_2} \lessapprox 10^{21}\,{\rm cm}^{-2}$. We therefore suggest that equation (24) overestimates $R_{\rm mol}$ at low pressures, possible as a consequence of the lower metallicity of this gas. To illustrate how this would change the model's CDDF, we show with the orange line the default model, except that we set the H_2 abundance of haloes with $M_{\rm h} < 10^{11}\,{\rm M}_\odot$ to zero (to account for the reasonable expectation that lower mass haloes have lower metallicity resulting in lower molecular fractions). Such a change still leads to an overestimate of the CDDF. If we further reduce the H_2 abundance of these haloes by a factor of 5, we obtain the orange dotted line, which now agrees well with the data. From this comparison, we conclude that, in so far as our model is actually applicable to molecules, low-density halo gas needs to be considerable less molecule rich than what a naive extrapolation of equation (24) would suggest. A recent comparison of alternative models for molecule formation that include the effects of metallicity is presented by Schäbe et al. (2020).

2.6 $\Omega_{\rm H\,I}$, $\Omega_{\rm H_2}$, and their evolution

Given the CDDF and the molecular fraction in haloes, we can integrate over column density to compute the fraction of the cosmological mass that is in neutral and molecular gas in units of the critical density,

$$\Omega_{\rm H\,I} = \frac{H_0\,\mu\,m_{\rm H}}{c\,\rho_{\rm c}} \int_0^\infty N_{\rm H\,I}\,f(N_{\rm H\,I})\,{\rm d}N_{\rm H\,I}$$

$$\Omega_{\rm H_2} = \frac{H_0\,\mu\,m_{\rm H}}{c\,\rho_{\rm c}} \int_0^\infty (2N_{\rm H_2})\,f(N_{\rm H_2})\,{\rm d}N_{\rm H_2}. \quad (27)$$

Here, $\mu = 1.3$ is the mean molecular weight per particle in units of the proton mass, $m_{\rm H}$, to account for helium and other elements, and the factor of 2 in the expression for $\Omega_{\rm H_2}$ counts the two hydrogen atoms per H_2 molecule.[12] The predictions for these two quantities are illustrated in Fig. 8.

Panel (a) of Fig. 8 repeats the H I CDDF from Fig. 2 at two redshifts (dotted lines), but also shows the CDDF corrected for molecules as discussed in the previous section (solid lines). The onset of H_2 introduces a cut-off in the CDDF that is particularly sharp at $z = 2$. Over most of the observed range (yellow line connecting error bars is the data from Noterdaeme et al. 2012), the impact of including molecule formation is small (see also Schaye 2001).

In panel (b) of Fig. 8, we plot the cumulative mass density in neutral in units of $\rho_{\rm c}$, $\Omega_{\rm H\,I}(< N_{\rm H\,I})$, at two redshifts (different colours)

[12]Notice that this is the traditional definition of $\Omega_{\rm H\,I}$: the cosmological mean density in gas that is mostly neutral – as opposed to the mass density of H I – in units of $\rho_{\rm c}$.

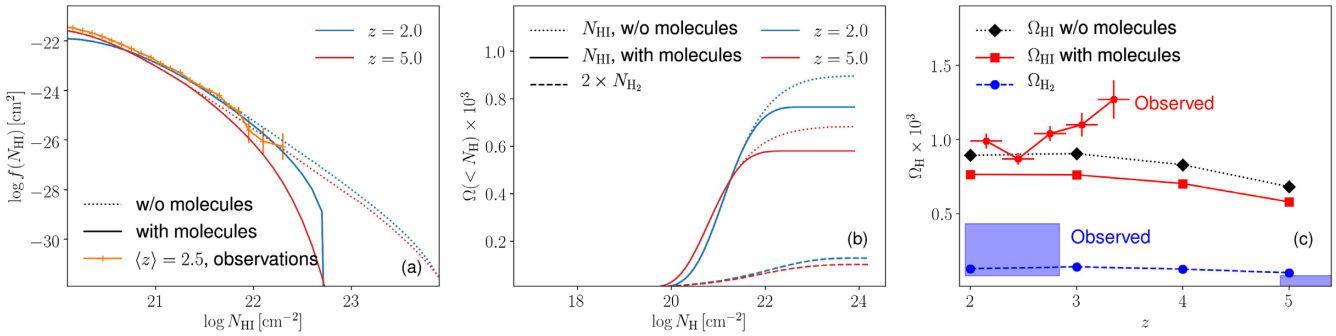

Figure 8. Density of neutral and molecular gas in units of the critical density. Panel (a): the model's H I CDDF at two redshifts (colours) when molecules are neglected (dotted line) and when molecules are included (solid line). The yellow line connecting error bars is the observed CDDF from Noterdaeme et al. (2012). Panel (b): as in panel (a), but plotting the cumulative fraction of gas in absorbers with column density $N_{\rm H} \le N_{\rm H\,I}$. The dashed lines correspond to the cumulative fraction of mass in molecular gas in absorbers with $N_{\rm H} \le 2N_{\rm H_2}$. Panel (c): mass density in neutral gas in units of the critical density, equation (33), for the model when molecules are included (red squares connected with a solid line) and when molecules are not included (black diamonds connected with a dotted line). The red line connecting error bars is the observed values from Noterdaeme et al. (2012). Circles connected by a dashed line refer to $\Omega_{\rm H_2}$, defined in equation (33); the filled blue squares are $\Omega_{\rm H_2}$ from the COLDz survey (Riechers et al. 2019).

and with or without including H_2 formation (solid and dotted lines, respectively). This panel demonstrates that $\Omega_{\rm H\,I}$ is dominated by gas in sub-DLAs and DLAs, as is well known. The panel also shows $\Omega_{\rm H_2}$ at the same two redshifts as dashed lines. There is little evolution in $\Omega_{\rm H_2}$ and $\Omega_{\rm H_2} \ll \Omega_{\rm H\,I}$ – therefore, including or excluding molecules makes less than ∼20 per cent difference to $\Omega_{\rm H\,I}$.

In panel (c) of Fig. 8, we plot the evolution of $\Omega_{\rm H\,I}$ (solid and dotted lines show the model including or excluding molecules, respectively), compared to the data of Noterdaeme et al. (2012). The model prediction is within 20 per cent of the observed value. Within the observational error bars, there is little evidence for evolution in the data as has been stressed by, e.g. Prochaska & Wolfe (2009). That panel also compares the predicted value of $\Omega_{\rm H_2}$ (blue circles connected by a dashed line) to the value reported by Riechers et al. (2019) from the COLDz survey (the blue filled rectangles, which correspond to the green error boxes in fig. 5 of Riechers et al. 2019). Given the relative simplicity of the model, the prediction is in relatively good agreement with the data. There is a hint that the evolution in the data is stronger than that in the model.

In models in which H I is mostly associated with the ISM of galaxies, the non-evolution of $\Omega_{\rm H\,I}$ over the redshift range $z = 5$–2 is surprising because the galaxy stellar mass function builds up significantly over this interval. If H I is the gas reservoir associated with galaxies, then we might expect $\Omega_{\rm H\,I}$ and $\Omega_\star$ (the cosmological mass density in stars divided by $\rho_{\rm c}$) to evolve in tandem – but they do not; see also Péroux et al. (2012). However, in the current model, most of the H I mass is actively accreting on to haloes rather than a reservoir that is being built up. As gas accretes on to a halo, it is initially highly ionized and hence does not contribute to $\Omega_{\rm H\,I}$. Once gas flows past the ionization front, $r < r_{\rm I}$ from equation (8), it becomes neutral. Even further in, $r < r_{\rm H_2}$, the radius where $R_{\rm mol}$ from equation (24) becomes ∼1, gas becomes molecular. This means that the cosmological mean density of H I, $\rho_{\rm H\,I} = \Omega_{\rm H\,I}\,\rho_{\rm c}/\mu$, is due to gas in haloes at a distance from the centre $r_{\rm H_2} < r < r_{\rm I}$. We can compute the evolution of the cosmological density of such gas as follows.

We first notice from panel (b) in Fig. 8 that $\Omega_{\rm H\,I}$ is dominated by gas with neutral fraction $x \approx 1$. This means that its numerical value does not depend (strongly) on the radial distribution of gas in haloes. Indeed, if instead $\Omega_{\rm H\,I}$ were to be dominated by the small neutral fraction in highly ionized gas for which $n_{\rm H\,I} \propto n_{\rm H}^2$ according to equation (4), then $\Omega_{\rm H\,I}$ would depend strongly on the radial density profile, $n_{\rm H}(r)$. Since we concluded that $\Omega_{\rm H\,I}$ does not depend on the radial distribution (as long as molecules can be neglected as well), $\rho_{\rm H\,I}$ should be related to the rate at which mass collapses into haloes that contain DLAs, i.e. those with halo mass $M_{\rm h} > M_{\rm h,\,crit}$. This means that we should be able to compute $\Omega_{\rm H\,I}$ directly from the rate of collapse into haloes without computing the CDDF first. We do so in the following.

We compute the collapsed fraction in haloes that host DLAs as the integral

$$\Omega_{\rm h} \equiv \frac{1}{\rho_{\rm c}} \int_{\log M_{\rm h,crit}}^{\infty} M_{\rm h}\,\frac{{\rm d}n}{{\rm d}\log M_{\rm h}}\,{\rm d}\log M_{\rm h}, \tag{28}$$

where in practice we integrate to an upper limit of $M_{\rm h} = 10^{13}\,{\rm M}_\odot$. This does not affect the results here, since the halo mass function is already decreasing exponentially well before that. We evaluate the integral in equation (28) numerically, computing ${\rm d}n/{\rm dlog}\,M_{\rm h}$ with the COLOSSUS tool of Diemer (2018). The result is plotted in the top panel of Fig. 9, together with the Taylor-series fit

$$\ln\left(\frac{\Omega_{\rm h}(z)}{0.065}\right) = -0.22(z-2) - 0.05(z-2)^2 + 0.0008(z-2)^3, \tag{29}$$

from which we compute that

$$\frac{{\rm d}\Omega_{\rm h}}{{\rm d}z} \approx -0.015(1 + 0.23\,(z-2) - 0.18\,(z-2)^2 + \cdots), \tag{30}$$

and ${\rm d}\Omega_{\rm h}/{\rm d}z \approx -0.015$ is constant to within ∼20 per cent from $z = 2$ to 4.

Our reasoning for the computation of $\Omega_{\rm H\,I}$, given ${\rm d}\Omega_{\rm h}/{\rm d}t = \dot{z}\,{\rm d}\Omega_{\rm h}/{\rm d}z$, goes as follows. Gas accretes on to haloes that host DLAs at a rate $\omega_{\rm b}\,{\rm d}\Omega_{\rm h}/{\rm d}t$, where the factor $\omega_{\rm b} \equiv \Omega_{\rm b}/\Omega_{\rm m}$ accounts for the gas fraction of the accreting matter. This accreting gas is observable as H I over a fraction, η, of the time τ it takes to flow from the virial radius of the halo, $r = R_{\rm h}$, to the centre, $r = 0$. We can estimate τ in two ways, which should give approximately the same answer. We can set $\tau = \tau_{\rm dyn}$, the dynamical time of the halo, or we can set $\tau = \tau_{\rm acc} \equiv R_{\rm h}/v_{\rm r}$, the 'accretion time' of the halo, with the radial velocity of the gas taken from equation (21).

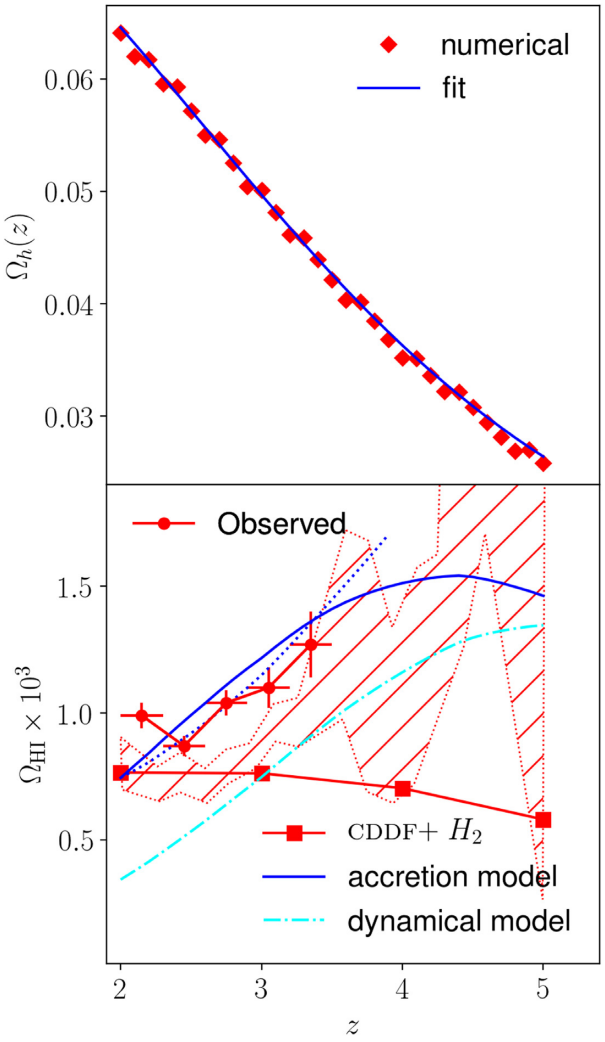

Figure 9. Upper panel: Evolution of the collapsed fraction, equation (28), computed numerically (red diamonds) and the fit from equation (29) (blue line). Lower panel: Evolution of $\Omega_{\rm H\,I}$. The red squares connected with a solid line and red line connecting error bars are, respectively, the model's evolution and the observed evolution, repeated from Fig. 8, and the red hashed region is the observed evolution from Bird, Garnett & Ho (2017). The cyan dash–dotted line and blue solid line assume that H I gas is observable as it accretes on to halo for a fraction $\eta = r_{\rm I}/R_{\rm h}$ of the flow time, equation (33), using the dynamical time ($\tau = \tau_{\rm dyn}$, equation 31) or the accretion time ($\tau = \tau_{\rm acc}$, equation 32), respectively. The blue dotted line is $\propto\eta(z)$, equation (34).

The dynamical time of the halo, $\tau_{\rm dyn}$, is approximately

$$\tau_{\rm dyn} = \frac{1}{({\rm G}\bar{\rho}_{\rm h})^{1/2}} = \left(\frac{8\pi}{600}\right)^{1/2} \frac{1}{H(z)}, \tag{31}$$

where the second step sets the mean density $\bar{\rho}_{\rm h}$ within $R_{\rm h}$ to 200 times the critical density (e.g. Mo et al. 1998). The accretion time of the halo, $\tau_{\rm acc}$, is

$$\tau_{\rm acc} \equiv \frac{R_{\rm h}}{v_r} = \left(\frac{{\rm d}\ln m_{\rm h}}{{\rm d}z}\dot{z}\right)^{-1} \approx \frac{1.33}{(1+z)H(z)}, \tag{32}$$

where we used equation (2) for the halo growth rate taking the numerical value $b = 0.75$ from Correa et al. (2015a). Our result is approximate in that we have set $\alpha = 2$ to calculate the halo's gas mass. Finally, the fraction of time that the gas is observable as H I should be approximately[13] $\eta \approx r_{\rm I}/R_{\rm h}$, the ratio of the radius of the ionization front ($r_{\rm I}$) – within which the gas is neutral – over the viral radius ($R_{\rm h}$).

Given this reasoning, we compute $\Omega_{\rm H\,I}$ as

$$\Omega_{\rm H\,I} = \left(\omega_{\rm b}\frac{{\rm d}\Omega_{\rm h}}{{\rm d}t}\right) \times (\eta\,\tau), \tag{33}$$

where $\tau = \tau_{\rm dyn}$ or $\tau = \tau_{\rm acc}$.

This equation forecasts that $\Omega_{\rm H\,I}$ depends relatively weakly on redshift. Indeed, taking $\tau = \tau_{\rm acc}$ we find that $\Omega_{\rm H\,I}(z) \propto \eta(z)\,(-{\rm d}\Omega_{\rm h}/{\rm d}z)$. Given that ${\rm d}\Omega_{\rm h}/{\rm d}z$ is approximately constant, the redshift dependence of $\Omega_{\rm H\,I}$ is mostly due to that of $\eta(z)$, which we discuss in more detail below. The reason for the lack of evolution is illuminating: It occurs because the rate of collapse into haloes is approximately inversely proportional to the accretion time of those haloes. Therefore, the product, $({\rm d}\Omega_{\rm h}/{\rm d}t)\,\tau_{\rm acc}$, is almost constant. This is the main reason for the lack of evolution in $\Omega_{\rm H\,I}$ in the current model.

We examine the evolution of η starting from equation (8),

$$\eta(z) \approx 0.25\left(\frac{(n_{\rm H,0}(z)/n_{\rm H,0}(2))^2\,(R_{\rm h}(z)/R_{\rm h}(2))}{\Gamma(z)/\,\Gamma(2)}\right)^{1/(2\alpha-1)}$$
$$\approx 0.25\frac{((1+z)/3)^{5/(2\alpha-1)}}{(\Gamma(z)/\,\Gamma(2))^{1/(2\alpha-1)}}. \tag{34}$$

We used $z = 2$ as the reference point, reading the value of $\eta(z=2) \approx 0.25$ for a halo with a mass of $M_{\rm h} = 10^{11}\,{\rm M}_\odot$ from Fig. 1. The virial radius of a halo with given mass decreases with z as $R_{\rm h} \propto 1/(1+z)$, whereas the density of the halo increases as $\propto(1+z)^3$. As a result $r_{\rm I}$ increases whereas $R_{\rm h}$ decreases with z. This evolution, combined with the evolution of Γ, causes the ratio $r_{\rm I}/R_{\rm h}$ to increase with z.

The numerical values we obtain are

$$\Omega_{\rm H\,I}(z=2) = \begin{cases} 0.74\times10^{-3} & \text{for } \tau = \tau_{\rm acc}, \\ 0.34\times10^{-3} & \text{for } \tau = \tau_{\rm dyn}. \end{cases} \tag{35}$$

The predicted evolution for both models is plotted in the lower panel of Fig. 9 (solid line: accretion model that uses $\tau = \tau_{\rm acc}$, dash–dot line: dynamical model that uses $\tau = \tau_{\rm dyn}$). The value obtained for the accretion model [$\Omega_{\rm H\,I}(z=2) = 0.75\times10^{-3}$] agrees very well with that obtained by integrating the $z = 2$ CDDF [$\Omega_{\rm H\,I}(z=2) = 0.77\times10^{-3}$] for the full model (solid squares connected by a red line) as well as the value inferred observationally by Noterdaeme et al. (2012) (solid red line connecting error bars [$\Omega_{\rm H\,I}(z=2.2) = (0.99\pm0.05)\times10^{-3}$], repeated from Fig. 8 in the lower panel of Fig. 9. The dynamical model underestimates $\Omega_{\rm H\,I}$ by a factor of $\sim$2.

We stress that these models are meant to reproduce the full model, shown as red squares connected with a solid line. The stronger evolution in the accretion model compared to the full model is due to the stronger evolution in $\eta(z)$ in the former. This is demonstrated by the blue dotted line, which is $\propto\eta(z)$ – it captures the evolution of the accretion model well. What the accretion model does not capture is that, at higher z, the CDDF and hence $\Omega_{\rm H\,I}$ are dominated by lower mass haloes. Such lower mass haloes have lower values of η. The accretion model does not account for this evolution of the DLA halo mass function.

[13]For a $1/r^2$ density distribution – which is close to the radial profile that we assume when taking $\alpha = 2.2$ – the enclosed mass in a *sphere* of radius r is proportional to r. However, here we need the mass enclosed in a circular aperture. Since we take a single value of η, whereas in reality we should take the average, weighing each halo mass with its cross-section, we think this approximation is good enough to understand the scaling of $\Omega_{\rm H\,I}$.

In summary, the value of $\Omega_{\rm H\,I}$ obtained by integrating the model CDDF agrees well with the value observed by Noterdaeme et al. (2012). Neither model nor data evolve strongly with redshift. In the model, H I gas is accreting on to haloes. We discussed how such an accretion model can be derived directly without making reference to the CDDF, equation (33). In this accretion model, the relative constancy of $\Omega_{\rm H\,I}$ results mostly from the fact that the accretion rate scales $\propto H(z)$ whereas the dynamical time of a halo scales $\propto 1/H(z)$ so that $\Omega_{\rm H\,I}$, which is proportional to their product, depends weakly on z.

3 DISCUSSION

We have made several simplifications in developing the simple model for predicting the absorption properties of gas as it accretes on to haloes and feeds a central galaxy. We briefly discuss their impact and how they could be improved.

(i) *Spherical accretion*: Numerical simulations show convincingly that cold gas accretes on to haloes in the form of *filaments* rather than spherically symmetric (e.g. Fumagalli et al. 2011; Cen 2012; Bird et al. 2014; Rahmati et al. 2015; van de Voort et al. 2019). Observational evidence for such filamentary accretion is mounting (e.g. Fumagalli et al. 2017). At the very least, the accreting gas also has angular momentum that will affect how it accretes. In addition, galactic outflows driven by energy injected in the interstellar medium are a major ingredient in simulations of galaxy formation (see e.g. Somerville & Davé 2015, for a review). Such outflows must, at some level, impact the accretion of gas. Finally, as gas accretes on to the galaxy, it eventually must encounter an accretion shock. Assuming that gas accretion is spherical, as we have done in this paper, is clearly a major simplification. One reason we suggest that this may not be as unreasonable as it looks at first sight is that a major fraction of the DLA cross-section of gas in a halo occurs relative far out. That accreting gas may not be affected so much by angular momentum or bipolar galactic outflows. In addition, provided that the halo mass is low, the location of any accretion shock may be relatively close to the galaxy, in which case it does not strongly affect the DLA cross-section. All these processes are likely to affect the CDDF at higher values of the column density. There is support for this view from the simulations by Altay et al. (2011), who show that the CDDF is little affected by feedback for columns $N_{\rm H\,I} \leq 10^{21.5}\,{\rm cm}^{-2}$, but there is increasingly significant impact at higher column densities.

(ii) *H i in the central galaxy*: At the centre of the halo, some fraction of the accreted gas will remain in the form of H I in the galaxy, with star formation occurring in molecular gas. We have not accounted for such a 'reservoir' of gas, but did try to account for H_2 formation. For the model to be viable, the majority of the accreted gas must therefore be ejected again in the form of a galactic wind, rather than be contained in the galaxy, and moreover this wind should not itself contribute significantly to H I in absorption. The galaxy formation model by Sharma & Theuns (2020) makes it plausible that the galactic outflow rate traces the accretion rate, rather than building a gas reservoir in the galaxy. Most models of galaxy formation appeal to strong outflows; see e.g. Somerville & Davé (2015) for a recent review.

(iii) *Cosmological accretion*: We assumed that the matter that accretes on to haloes does so purely in the form of cosmological accretion with the cosmic baryon fraction. In reality, some fraction of baryons will have collapsed into smaller galaxies before, and some may have been ejected by feedback. Conversely, a fraction of the gas accreting on to the halo may have been ejected by the halo's galaxy previously and is now being 'recycled'. The extent to which this affects accretion on to haloes likely depends on mass and redshift, Garratt-Smithson et al. (2020) and Wright et al. (2020) examined some of these effects in the EAGLE simulations at $z \lessapprox 2$.

(iv) *Recombinations*: We used the 'case-B' recombination rate for hydrogen, appropriate in situations where a recombination directly to the ground state releases a photon that ionizes a neutral hydrogen in the immediate vicinity – also called the 'on-the-spot approximation'. This might be a good approximation inside and close to the ionization front, but will underestimate recombinations in the highly ionized outskirts of the gas profile. At $T = 10^4$ K, the case-A (total) recombination rate is $\approx$1.6 times higher than the case-B value. Improving this aspect might increase the number of LLSs and sub-DLAs by a small fraction, and could also affect the shape of the knee in the CDDF. In a similar vein, we also neglected spectral hardening, which could also impact the shape of the knee in the CDDF. Both effects were included in the URCHIN radiative transfer calculations of Altay et al. (2011) to which we compared our model in Fig. 3. In particular, URCHIN switches between case-A and case-B recombination rates when the shielding optical depth $\tau > 1$ (Altay & Theuns 2013). It also uses 100 frequency bins to account for spectral hardening. We also assumed that the accreting gas remains isothermal at $T = 10^4$ K. The temperature–density relation seen in cosmological simulations shows that IGM gas instead heats as gas accretes from $T \sim 10^4$ to $\approx 10^{4.4}$ K before cooling back to 10^4 K (see, for example, fig. 2 in Theuns et al. 1998). This increase in T decreases the recombination rate by a factor of $\approx$2.2. To get this temperature evolution right requires radiation-hydrodynamical simulations, which can simultaneously account for shielding from the UV background and its impact on the cooling and heating rates of the accreting gas. We also neglected any impact of radiation from the central galaxies on the DLA (see e.g. Rahmati et al. 2013).

(v) *DLA line widths*: A characteristic feature of the line shape of low-ionization metal absorption associated with DLAs is that the strongest absorption tends to occur at the edges of the absorption systems ('edge-leading spectra'; Neeleman et al. 2013). Simulations seem to be able to reproduce this (e.g. Bird et al. 2015). We have not examined whether our model is consistent with this.

(vi) *Molecules*: At face value, the agreement between the model prediction and observations of the molecular CDDF is not very good, with the model overpredicting $N_{\rm H_2}$ by a significant amount. It would be interesting to examine how well simulations do. It seems reasonable to expect that a model that accounts better for the impact of metals on the H_2 abundance would improve the agreement with the data. In any case, we expect that some model features would still emerge, such as the flattening of the $N_{\rm H\,I}$ column at small impact parameter and the associated bend in the H I CDDF at high $N_{\rm H\,I}$.

4 SUMMARY AND CONCLUSIONS

The high star formation rate measured in galaxies at $z \gtrapprox 2$ is mostly fuelled by cosmological accretion; however, observing this accreting gas directly has proved to be challenging (e.g. Fumagalli et al. 2011). In this paper, we have examined a simple model for cosmological accretion on to dark matter haloes, based on the similarity solution of Bertschinger (1985), and including approximate radiative transfer to account for self-shielding from an ambient ionizing background taken from Haardt & Madau (2012). In this model, the accreting gas gives rise to LLSs in the surroundings and outskirts of the halo where it is highly ionized, and to damped Lyman-α systems (DLAs) in the inner halo where the gas is mostly neutral. The resulting CDDF is in excellent agreement with the data (Fig. 2). To the extent that the

model captures accretion of gas on to haloes, it seems that we have been observing the accreting gas that fuels star formation all along.

The shape of the CDDF reflects that of the power-law radial distribution of the gas, $n_{\rm H}(r) \propto r^{-\alpha}$, with $\alpha \approx 2.2$. The reason is that the density profile is self-similar and hence the same for all haloes. In the LLS regime, the slope of the CDDF is $f(N_{\rm H\,I}) \propto N_{\rm H\,I}^{2/(1-2\alpha)-1} \propto N_{\rm H\,I}^{-1.6}$, whereas in the DLA regime it is $f(N_{\rm H\,I}) \propto N_{\rm H\,I}^{2/(1-\alpha)-1} \propto N_{\rm H\,I}^{-2.7}$. Our analytical expression explains why haloes contribute about equally to the CDDF over a large range of halo masses, $M_{\rm h} = 10^{10}$–10^{12} M$_\odot$ (lower mass haloes are more numerous but their cross-section is smaller; see equation 14) as well as why the amplitude of the CDDF evolves so little with redshift (although haloes become more abundant at lower z, their cross-section decreases; see equation 17). We also explain the origin of a lower mass cut-off [reionization introduces a redshift-dependent critical mass, $M_{\rm crit}(z)$, below which haloes lose their gas; Okamoto et al. (2008)] and why high-mass haloes do not contribute more to DLAs (the exponential cut-off in the halo mass function).

The relative contribution of haloes of a given mass to the CDDF does evolve in the sub-DLA regime ($N_{\rm H\,I} \lesssim 10^{20}$ cm^{-2}), where lower mass halo contribute more at higher z. This leads to a change in the location of the 'knee' in the CDDF – the transition from LLS to DLAs – with the knee shifting to lower values of $N_{\rm H\,I}$ at higher z (see Fig. 2). This shift is caused by the evolution of the critical mass $M_{\rm crit}(z)$, which becomes smaller at higher z. Detecting such an evolution in the data might constrain the evolution of this critical mass.

Computing the differential contribution of haloes of a given mass to the CDDF allows us to evaluate the DLA bias (Section 2.3), which agrees well with the observed value, as well as the distribution of DLA line widths, v_{90} (Section 2.4). We assumed that accreting gas falls in radially, at a rate consistent with the cosmological accretion rate, and weigh the infall velocity with the cosine of the angle with the line of sight. For a given halo, this introduces a relation between column density and v_{90}, because at a smaller impact parameter, the DLA column density is higher and the gas flows increasingly parallel to the line of sight so that v_{90} is larger. Integrating over all haloes yields the distribution of v_{90}, which has a relatively sharp cut-off at $\sim$30 km s^{-1} and a long tail towards high values of v_{90} (Fig. 6). The sharp cut-off is related to the value of $M_{\rm crit}(z)$. The extended tail results from DLA sightlines that intersect rare massive haloes at an unusually small impact parameter.

We used the model of Blitz & Rosolowsky (2006) to attempt to compute where the DLA gas turns molecular (Section 2.5). This overpredicts the H_2 CDDF, especially at low $N_{\rm H_2}$, but does reasonably well at higher column densities. The model predicts a maximum value of $N_{\rm H\,I}$ caused by high-column-density gas turning increasingly molecular (see also Schaye 2001; Erkal, Gnedin & Kravtsov 2012). The value of this maximum column density depends on halo mass. The presence of such a maximum leads to a downturn in the H I CDDF. Notwithstanding the superb statistics of the observed CDDF (Noterdaeme et al. 2012), such a downturn is not yet clearly detected.

Integrating over the CDDF yields the fraction of the mass in the Universe that is in neutral gas, $\Omega_{\rm H\,I}$, or in molecular gas, $\Omega_{\rm H_2}$ (Section 2.6). The model prediction agrees well with observations (Fig. 8). We presented a model that captures the accretion origin of the H I gas, and which reproduces well the results of the full model. This simpler model elucidates why $\Omega_{\rm H\,I}$ evolves so slowly, as observed. The underlying reason is that the accretion rate on to haloes increases with redshift at the same rate as the flow time-scale of the gas within haloes decreases. Since $\Omega_{\rm H\,I}$ is proportional to the product of these (equation 33), it evolves slowly.

It has long be posited that the H I seen in absorption fuels star formation in galaxies (e.g. Wolfe, Gawiser & Prochaska 2005). Within this interpretation, the fact that the mean H I density, $\Omega_{\rm H\,I}$, evolves weakly with z whereas the star formation rate density evolves strongly is puzzling. The solution to the puzzle as discussed in this paper is twofold: First, the observed H I is dominated by gas accreting on to haloes rather than a reservoir of gas in the galaxy's interstellar medium (ISM). Although a sightline through a galaxy likely produces a DLA, the reverse is not true: *Every galaxy is a* DLA*, but not every* DLA *is a galaxy*. The accreting gas is in the form of H I for a fraction of time as it accretes on to a halo. This explains why the accretion rate (and hence also the star formation rate) can vary with redshift while $\Omega_{\rm H\,I}$ remains approximately constant. Secondly, as the H I gas gets close to the centre and enters the galaxy's ISM, it becomes molecular, some fraction forms stars, but the majority is ejected in the form of a galaxy-wide outflow. This implies that any 'reservoir' of H I in the ISM of the galaxy remains small.

In short, we claim that LLSs and DLAs are both related to the accretion of gas on to haloes, and only a small fraction of this accreted gas fuels star formation in galaxies. This simple picture is consistent with the observed properties of LLS and DLAs.

ACKNOWLEDGEMENTS

I want to thank J. Fynbo for encouraging me to start this project, M. Fumagalli and R. Cooke for excellent suggestions, and an anonymous referee for constructive comments. This work was supported by STFC grant ST/P000541/1 and used the DiRAC Data Centric system at Durham University, operated by the Institute for Computational Cosmology on behalf of the STFC DiRAC HPC Facility (www.dirac.ac.uk). This equipment was funded by BIS National E-infrastructure capital grant ST/K00042X/1, STFC capital grants ST/H008519/1 and ST/K00087X/1, STFC DiRAC Operations grant ST/K003267/1, and Durham University. DiRAC is part of the UK's National E-Infrastructure.

DATA AVAILABILITY

No new data were generated or analysed in support of this research.

REFERENCES

Ahn C. P. et al., 2012, ApJS, 203, 21
Alam S. et al., 2015, ApJS, 219, 12
Altay G., Theuns T., 2013, MNRAS, 434, 748
Altay G., Theuns T., Schaye J., Crighton N. H. M., Dalla Vecchia C., 2011, ApJ, 737, L37
Altay G., Theuns T., Schaye J., Booth C. M., Dalla Vecchia C., 2013, MNRAS, 436, 2689
Bahcall J. N., Peebles P. J. E., 1969, ApJ, 156, L7
Balashev S. A., Noterdaeme P., 2018, MNRAS, 478, L7
Beaver E. A., Burbidge E. M., McIlwain C. E., Epps H. W., Strittmatter P. A., 1972, ApJ, 178, 95
Becker G. D., Bolton J. S., 2013, MNRAS, 436, 1023
Bertschinger E., 1985, ApJS, 58, 39
Bird S., Vogelsberger M., Haehnelt M., Sijacki D., Genel S., Torrey P., Springel V., Hernquist L., 2014, MNRAS, 445, 2313
Bird S., Haehnelt M., Neeleman M., Genel S., Vogelsberger M., Hernquist L., 2015, MNRAS, 447, 1834
Bird S., Garnett R., Ho S., 2017, MNRAS, 466, 2111
Blitz L., Rosolowsky E., 2006, ApJ, 650, 933
Cen R., 2012, ApJ, 748, 121
Correa C. A., Wyithe J. S. B., Schaye J., Duffy A. R., 2015a, MNRAS, 450, 1514

Correa C. A., Wyithe J. S. B., Schaye J., Duffy A. R., 2015b, MNRAS, 450, 1521
Crain R. A. et al., 2017, MNRAS, 464, 4204
Davis M., Efstathiou G., Frenk C. S., White S. D. M., 1985, ApJ, 292, 371
Dekel A. et al., 2009, Nature, 457, 451
Diemer B., 2018, ApJS, 239, 35
Di Gioia S., Cristiani S., De Lucia G., Xie L., 2020, MNRAS, 497, 2469
Erkal D., Gnedin N. Y., Kravtsov A. V., 2012, ApJ, 761, 54
Faucher-Giguère C.-A., Kereš D., 2011, MNRAS, 412, L118
Faucher-Giguère C.-A., Hopkins P. F., Kereš D., Muratov A. L., Quataert E., Murray N., 2015, MNRAS, 449, 987
Font-Ribera A. et al., 2012, J. Cosmol. Astropart. Phys., 2012, 059
Fumagalli M., Prochaska J. X., Kasen D., Dekel A., Ceverino D., Primack J. R., 2011, MNRAS, 418, 1796
Fumagalli M., O'Meara J. M., Prochaska J. X., Worseck G., 2013, ApJ, 775, 78
Fumagalli M., O'Meara J. M., Prochaska J. X., Rafelski M., Kanekar N., 2015, MNRAS, 446, 3178
Fumagalli M. et al., 2017, MNRAS, 471, 3686
Fynbo J. P. U., Prochaska J. X., Sommer-Larsen J., Dessauges-Zavadsky M., Møller P., 2008, ApJ, 683, 321
Fynbo J. P. U. et al., 2010, MNRAS, 408, 2128
Garratt-Smithson L., Power C., Lagos C. d. P., Stevens A. R. H., Allison J. R., Sadler E. M., 2020, preprint(arXiv:2008.09302)
Haardt F., Madau P., 2012, ApJ, 746, 125
Ho M.-F., Bird S., Garnett R., 2020, MNRAS, 496, 5436
Kaiser N., 1984, ApJ, 284, L9
Kereš D., Katz N., Weinberg D. H., Davé R., 2005, MNRAS, 363, 2
Krogager J. K., Møller P., Fynbo J. P. U., Noterdaeme P., 2017, MNRAS, 469, 2959
Krogager J.-K., Møller P., Christensen L. B., Noterdaeme P., Fynbo J. P. U., Freudling W., 2020, MNRAS, 495, 3014
Mackenzie R. et al., 2019, MNRAS, 487, 5070
McQuinn M., Oh S. P., Faucher-Giguère C.-A., 2011, ApJ, 743, 82
Maller A. H., Prochaska J. X., Somerville R. S., Primack J. R., 2001, MNRAS, 326, 1475
Mo H. J., Mao S., White S. D. M., 1998, MNRAS, 295, 319
Møller P., Fynbo J. P. U., Fall S. M., 2004, A&A, 422, L33
Nagamine K., Springel V., Hernquist L., 2004, MNRAS, 348, 421
Neeleman M., Wolfe A. M., Prochaska J. X., Rafelski M., 2013, ApJ, 769, 54
Noterdaeme P. et al., 2012, A&A, 547, L1
Okamoto T., Gao L., Theuns T., 2008, MNRAS, 390, 920
Padmanabhan H., Choudhury T. R., Refregier A., 2016, MNRAS, 458, 781
Pérez-Ràfols I. et al., 2018, MNRAS, 473, 3019
Péroux C., Howk J. C., 2020, ARA&A, 58, 363
Péroux C., Storrie-Lombardi L. J., McMahon R. G., Irwin M., Hook I. M., 2001, AJ, 121, 1799
Péroux C., Bouché N., Kulkarni V. P., York D. G., Vladilo G., 2012, MNRAS, 419, 3060
Péroux C. et al., 2016, MNRAS, 457, 903
Petitjean P., Bergeron J., Puget J. L., 1992, A&A, 265, 375
Planck Collaboration XVI, 2014, A&A, 571, A16
Pontzen A. et al., 2008, MNRAS, 390, 1349
Prochaska J. X., Wolfe A. M., 2009, ApJ, 696, 1543
Prochaska J. X., Gawiser E., Wolfe A. M., Castro S., Djorgovski S. G., 2003, ApJ, 595, L9
Prochaska J. X., Herbert-Fort S., Wolfe A. M., 2005, ApJ, 635, 123
Rahmati A., Schaye J., Pawlik A. H., Raičević M., 2013, MNRAS, 431, 2261
Rahmati A., Schaye J., Bower R. G., Crain R. A., Furlong M., Schaller M., Theuns T., 2015, MNRAS, 452, 2034
Rauch M., 1998, ARA&A, 36, 267
Reed D. S., Bower R., Frenk C. S., Jenkins A., Theuns T., 2007, MNRAS, 374, 2
Rhodin N. H. P., Agertz O., Christensen L., Renaud F., Fynbo J. P. U., 2019, MNRAS, 488, 3634
Riechers D. A. et al., 2019, ApJ, 872, 7
Sawala T. et al., 2015, MNRAS, 448, 2941
Schäbe A., Romano-Díaz E., Porciani C., Ludlow A. D., Tomassetti M., 2020, MNRAS, 497, 5008
Schaye J., 2001, ApJ, 562, L95
Schaye J. et al., 2010, MNRAS, 402, 1536
Schaye J. et al., 2015, MNRAS, 446, 521
Sharma M., Theuns T., 2020, MNRAS, 492, 2418
Somerville R. S., Davé R., 2015, ARA&A, 53, 51
Sommer-Larsen J., Fynbo J. P. U., 2017, MNRAS, 464, 2441
Sykes C., Fumagalli M., Cooke R., Theuns T., Benítez-Llambay A., 2019, MNRAS, 487, 609
Tescari E., Viel M., Tornatore L., Borgani S., 2009, MNRAS, 397, 411
Theuns T., Leonard A., Efstathiou G., Pearce F. R., Thomas P. A., 1998, MNRAS, 301, 478
Tinker J. L., Robertson B. E., Kravtsov A. V., Klypin A., Warren M. S., Yepes G., Gottlöber S., 2010, ApJ, 724, 878
van der Wel A. et al., 2014, ApJ, 788, 28
van de Voort F., Schaye J., Altay G., Theuns T., 2012, MNRAS, 421, 2809
van de Voort F., Springel V., Mandelker N., van den Bosch F. C., Pakmor R., 2019, MNRAS, 482, L85
Weymann R. J., Carswell R. F., Smith M. G., 1981, ARA&A, 19, 41
Wolfe A. M., Turnshek D. A., Smith H. E., Cohen R. D., 1986, ApJS, 61, 249
Wolfe A. M., Gawiser E., Prochaska J. X., 2005, ARA&A, 43, 861
Wright R. J., , , Lagos C. d. P., Power C., Mitchell P. D., 2020, MNRAS, 498, 1668
Zafar T., Péroux C., Popping A., Milliard B., Deharveng J. M., Frank S., 2013, A&A, 556, A141
Zheng Z., Miralda-Escudé J., 2002, ApJ, 568, L71
Zwaan M. A., Prochaska J. X., 2006, ApJ, 643, 675

This paper has been typeset from a TEX/LATEX file prepared by the author.